https://doi.org/10.5194/egusphere-2025-6209
Preprint. Discussion started: 21 January 2026

Evaluating the performance of a UAV-based in situ methane sensor for quantifying point source emissions

Noni van Ettinger[1], Steven M.A.C. van Heuven[1], Huilin Chen[1, 2]

[1]Centre for Isotope Research (CIO), Energy and Sustainability Institute Groningen (ESRIG), University of Groningen, the Netherlands

[2] Joint International Research Laboratory of Atmospheric and Earth System Sciences, School of Atmospheric Sciences, Nanjing University, Nanjing, China

Correspondence to: Noni van Ettinger (n.van.ettinger@rug.nl)

Competing interests: One author is a member of the editorial board of AMT

Abstract. Methane (CH_4) is the second most important greenhouse gas, and accurate quantification of its emissions is critical for mitigating climate change. In this study, we thoroughly evaluated the performance of an in situ CH_4 sensor (Axetris) for quantifying anthropogenic CH_4 emissions when deployed on an unmanned aerial vehicle (UAV). Sensor stability was assessed through laboratory tests under controlled and varying temperature conditions. Under stable conditions, the sensor achieved a precision of 63 ppb at 2 Hz. Furthermore, the tests revealed the necessity of temperature control and provided a water vapour correction term to ensure accurate measurements. Additionally, the sensor was used to quantify whole-farm CH_4 emissions, yielding a mean flux of 4.1 ± 1.6 gCH_4/s averaged over four flights. This mean flux was comparable to the value of 4.2 ± 1.1 gCH_4/s obtained from the established AirCore technique. Finally, an uncertainty analysis based on the Ornstein-Uhlenbeck method was used to determine the influence of various sources of uncertainty. This analysis revealed that both wind-related uncertainties and background determination can significantly increase the overall uncertainty when not properly constrained. Furthermore, instrumental errors play a dominant role for smaller fluxes, while meteorological uncertainties remain significant even with repeated flights. Nevertheless, careful flight planning, e.g., ensuring extensive sampling outside of the plume and comprehensive wind monitoring, can reduce these uncertainties. Overall, our results demonstrate that a cost-effective sensor can provide reliable CH_4 flux estimates with uncertainties comparable to those of established UAV-based systems.

1 Introduction

Methane (CH_4) is the second most important anthropogenic greenhouse gas (GHG) and has received increasing attention due to its relatively short atmospheric lifetime and strong global warming potential (GWP) compared to CO_2. The global average dry air mole fraction of CH_4 reached 1942 ppb in 2024 and is expected to increase in the coming years (WMO, 2025). Approximately 60% of the global CH_4 emissions are linked to human activities, primarily from agriculture, fossil fuel production and use, and waste disposal (Saunois et al., 2020). The observed rise in global CH_4 mole fraction is driven not only by anthropogenic sources but also by changes in natural CH_4

fluxes, influenced by ongoing climate change (Ciais et al., 2013). Reducing CH_4 emissions is essential for climate mitigation and represents a key strategy for limiting global warming to below 2 °C (UNEP & CCAC, 2021). To evaluate the effectiveness of mitigation efforts, monitoring CH_4 emissions and identifying their sources are critical.

Despite recent efforts, uncertainties of 20-35% remain in estimates of global annual anthropogenic CH_4 emissions (Saunois et al., 2020). These uncertainties arise from limitations in available data as well as underreporting and misreporting in national inventories. Current CH_4 emission inventories suffer from inconsistencies due to scarce observational data and methodological disparities. Given limitations in existing monitoring systems, approaches focusing on additional measurements and regional studies can help reduce uncertainties in top-down estimates (Saunois et al., 2020; Bousquet et al., 2018; Bruhwiler et al., 2017). Additionally, specific emission sources, such as manure and landfills, exhibit complex emission patterns with substantial diurnal and seasonal variability, making more frequent and reliable measurements necessary.

To address these gaps and uncertainties, cost-effective, scalable, and easily maintainable sensor technologies, coupled with robust monitoring methodologies for quantifying anthropogenic CH_4 emissions, are needed. These technologies can be used in more regional studies to evaluate the efficacy of mitigation strategies and monitor emission reductions at finer spatial resolutions (Saunois et al., 2020). International frameworks such as the United Nations Framework Convention on Climate Change (UNFCCC) support the implementation of unified methodologies to improve the accuracy of national inventories. Regular and systematic monitoring is vital for verifying mitigation outcomes and can help detect more fugitive emissions, which are often underrepresented in inventories (Erland et al., 2022).

Unmanned aerial vehicles (UAVs) have emerged as valuable tools for addressing data gaps in GHG emission monitoring. Recent advances in sensor technologies have enabled the integration of more lightweight instruments with UAV platforms. These systems offer advantages over alternative approaches (e.g., ground-based or satellite-based observations) by facilitating targeted emission sampling at finer spatial resolutions and bridging the observational gap between ground level and altitudes up to 120 meters (though UAVs are capable of flying much higher, regulations typically limit their max altitude). Furthermore, UAVs are versatile, easy to deploy and maintain, and have a relatively low implementation cost (Villa et al., 2016; Shaw et al., 2021).

Recent UAV-based GHG studies have employed three main sensor deployment strategies: (1) tethered systems connecting an UAV to a ground-based analyser (Shah et al., 2020); (2) semi-continuous sampling equipment (e.g., Active AirCore), mounted directly on UAVs for post-flight ground analysis (Andersen et al., 2018; Vinković et al., 2022; Leitner et al., 2023, Han et al., 2024); (3) real-time in situ sensors fully integrated into UAV platforms (Kunz et al. 2018; Allen et al., 2019; Tuszon et al., 2020; Scheutz et al., 2024). Although these techniques differ operationally, they all rely on the mass balance approach (MBA; Nathan et al., 2015; Vinković et al., 2022) or the inverse Gaussian approach (IGA; Andersen et al., 2021) for flux quantification. This study focuses on the MBA because it can directly convert atmospheric concentration measurements into fluxes.

While all flux quantification techniques introduce inherent uncertainties, wind conditions and spatial distribution of the flight track design consistently emerge as the most influential factors. In general, uncertainties in airborne flux estimates range from 20% to 75%. Still, they can exceed 100% under challenging conditions such as low wind speeds (<2 m/s), high wind direction variability (e.g. >30°), or non-uniform sampling (Vinković et al., 2022; Morales et al., 2021; Scheutz et al., 2024; Liu et al., 2024; Mohammadloo et al., 2025).

Instrumental or sensor precision is generally considered a minor factor compared to the factors mentioned above, underscoring the importance of investing in accurate wind measurements and thoughtful flight planning rather than prioritising high-precision sensors. Nonetheless, recent research has focused on developing increasingly lightweight and high-precision sensors (Tuszon et al., 2020; Kunz et al., 2018; Allen et al., 2019). While these advancements are valuable, their presumed high cost and maintenance demands limit their widespread deployment. Evidence suggests that low-cost, medium-precision sensors, when combined with accurate wind measurements and optimised flight planning, can achieve flux estimates with uncertainties comparable to those obtained using high-precision sensors.

In this study, we present and evaluate the performance of a low-cost, medium-precision CH_4 in situ sensor that meets key operational criteria. First, the sensor was characterised in the laboratory to optimise system performance and minimise drift. Following extensive testing, the sensor was deployed during a field campaign alongside the Active AirCore to quantify CH_4 emissions from a Dutch dairy farm, a site previously surveyed by Vinković et al. (2022). This enabled a direct comparison between flux estimates derived from our medium-precision sensor and those from the established Active AirCore technique, providing new insights into the role of measurement uncertainty in flux quantification. Finally, a statistical model was used to further investigate the influence of common sources of uncertainty.

2 Laboratory characterisation

Sensor characterisation is essential for improving sensor useability, as laboratory experiments provide insight into its behaviour under varying conditions. In this study, the standard operation of an in situ CH_4 sensor was characterised under stable laboratory conditions. A linearity test was performed to determine the sensor's response over a wide range of concentrations by comparing it to a high-precision reference analyser whose response is known to be linear. An Allan variance analysis provided information on the sensor's precision under baseline conditions (e.g., stable temperature, stable pressure, and no external vibrations), enabling direct comparison across various use cases and setups. The follow-up experiments focused on isolating the effect of different environmental factors on the sensor's output. Water vapour experiments were performed to determine the effect of water vapour on sensor readings. Additional Allan variance analyses were performed to compare the sensor’s performance under various conditions, e.g., active temperature control, laboratory and in-flight conditions.

https://doi.org/10.5194/egusphere-2025-6209
Preprint. Discussion started: 21 January 2026

2.1 The Axetris in situ methane sensor package

We developed a UAV-mounted sensor package incorporating a commercially available in situ CH_4 sensor (LGD-compact A CH_4; Axetris AG, Kaegiswil, Switzerland), hereafter referred to as the Axetris. The sensor is capable of real-time monitoring at a 2 Hz sampling frequency using a tuneable diode laser spectroscopy (TDLS) technique, which specifically targets the CH_4 absorption wavelength at ~1652 nm.

We integrated the Axetris onto a self-built printed circuit board (PCB) designed around an ESP32 microprocessor, enabling logging of data from the Axetris and ancillary sensors. The Axetris reports CH_4 mole fractions, the temperatures of the measurement cell and the interface PCB. Furthermore, the complete package includes a pressure sensor (AMSYS GmbH model 5915-1200-B) with a precision of ±0.36 hPa and a measuring range of 800-1200 hPa. A 1200 mAh, 7.4 V Li-ion battery pack powers the whole system. Ambient air was drawn through a filter (Rezist 30/ 5.0 PTFE-s; Whatman, Freiburg, Germany) into and through the sampling system using a micropump (NMP09; KNF, Freiburg, Germany) at a flow rate of 650 standard cubic centimetre per minute (sccm), ensuring rapid transfer of the sample to and through the measurement cell. With a sampling line volume of ~7 mL and an ambient-pressure cell volume of 19 mL, this configuration yields a time delay of less than 1 second for the sample to reach the measurement cell and a system response time constant of ~1.7 seconds (~4.2 seconds t_{90}).

The complete system was housed in a 20x20x10 cm polyethylene (PE) foam enclosure, yielding a relatively lightweight package (1.2 kg). The foam casing acted as a thermal insulator, helping to maintain a stable operating temperature for the analyser. The system had a wireless connection, which provided the ground time with real-time measurements and enabled remote control of critical functions.

To improve measurement quality, 1.1 m of low-power heating wire (Nc I 20; ThermoCoax, Suresnes, France) was coiled around the sensor head. This coil was used to maintain the measurement cell's temperature at a predetermined value (typically approximately 10 K above ambient), improving the system's thermal stability and mitigating erratic sensor behaviour caused by ambient temperature fluctuations. A PID controller controlled the duty cycle of the heating element, which used the measurement cell temperature (1 mK resolution, 2 Hz) as input. This setup regulated the temperature to within ±0.005 K from the set-point under lab conditions, and within 0.05 K during flight (Appendix A). Figure 1a presents a schematic of the complete Axetris package.

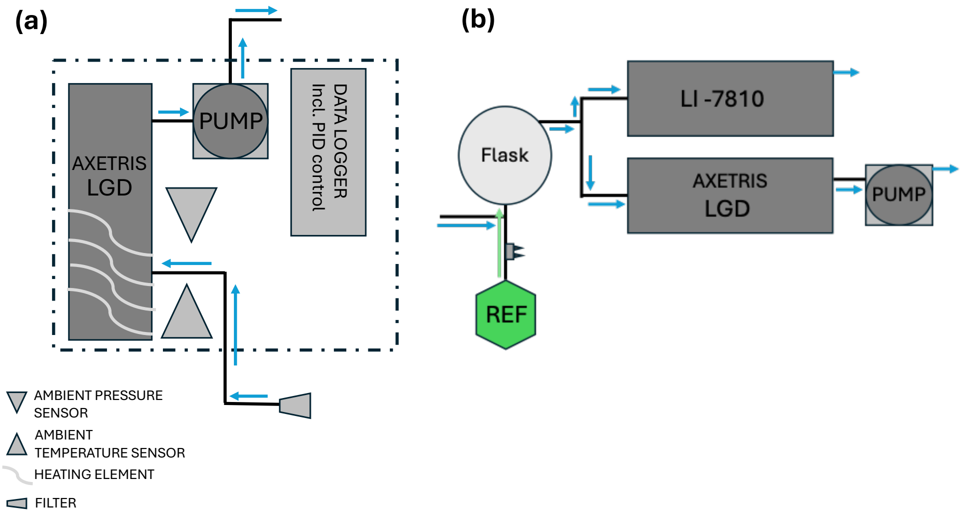

Figure 1: a) schematic overview of the Axetris package for UAV applications. The blue arrows show the airflow through the system during measurements. Components in the dotted and dashed lines enclosed area are integrated onto the PCB and enclosed in the PE foam. The datalogger communicates with the Axetris sensor and provides active control of the heating element, including setting and maintaining the desired temperature. b) Experimental overview for linearity test setup. First, the flask is filled with the reference gas, which has a high CH_4 concentration (indicated by the green arrow). Then, both systems start to sample the air from the flask, while ambient air was drawn in to mix with the high concentration (blue arrows), slowly decreasing the concentration in the flask.

2.2 LI-7810 trace gas analyser

The LI-7810 trace gas analyser (LI-COR Biosciences, Lincoln, USA) is a high-precision multi-gas analyser that provides continuous measurements of CH_4, CO_2, and H_2O in a durable, portable design. The LI-7810 uses optical feedback cavity enhanced absorption spectroscopy (OF-CEAS). It contains a 6.41 cm^3 optical cavity operating at standard conditions of 40 kPa (i.e., V_{eff}= ~ 2.5 cm^3) and 55 °C, and a flow rate of 250 sccm. For this study, the LI-7810 was equipped with a "low flow kit", which lowered the flow rate to ~70 sccm and changed the system's response time constant to approximately 2.3 seconds (~5.5s t_{90}).

The precision, accuracy, and linearity of the LI-7810 analyser under standard operating conditions were evaluated in an extensive report executed by ICOS (ICOS, 2020). From our laboratory tests, we found a 1-second precision of 0.1 ppb for CH_4 and 0.2 ppm for CO_2, respectively. The short-term drift over 24 hours was < 0.7 ppb for CH_4 and < 3 ppm for CO_2, respectively. The 1-second precision of the system operating at reduced flow was the same as under standard operating conditions.

https://doi.org/10.5194/egusphere-2025-6209
Preprint. Discussion started: 21 January 2026

2.3 Linearity of the Axetris

System linearity was verified by connecting both systems to a flask filled with a high CH_4 concentration (~81 ppm). The concentration inside the flask was then gradually reduced by allowing ambient air to enter, while the Axetris and the LI-7810 sampled it (see Figure 1b for experimental setup). The LI-7810 system linearity was confirmed by extensive laboratory tests (ICOS, 2020). These tests enabled direct comparison of the systems' response across a wide range of concentrations. Figure 1b shows an overview of the experimental setup.

The linearity test revealed strong agreement between the Axetris and LI-7810, with a correlation coefficient of 0.996. The linear equation between the two systems is as follows:

$$CH_{4\_Ax} = -142 + 1.001 CH_{4\_LIC}$$

The slope confirms linearity between the two systems, while the intercept indicates the bias between them. This bias (142 ppb) can be easily dealt with through calibration. The results confirm the reliability of the Axetris under controlled conditions and its ability to measure high CH_4 concentrations with strong linearity to the LI-7810 (Appendix B; Figure B1).

2.4 Water vapour corrections

Water vapour can significantly affect gas sensor readings in two ways: (1) by dilution of trace gas concentrations and (2) through more complex spectroscopic effects. The influence varies depending on the sensor type and the correction algorithms implemented by the sensor manufacturer (Butenhoff & Khalil, 2002). To characterise the effect of water vapour on the Axetris response and derive an empirical correction, we conducted a controlled water-droplet test.

While performing the water droplet test, the Axetris and the LI-7810 sampled air from a gas cylinder containing a high concentration of CH_4 (~81 ppm). A Swagelok compartment containing a wet paper towel was placed between the sampling lines to introduce water vapour into the otherwise dry gas stream (Appendix C; Figure C1 for experimental set-up). The compartment was gradually heated using a hairdryer to increase humidity levels, measured with the LI-7810. Water vapour concentrations ranged from 0.06 % to 1.4 %, corresponding to relative humidity of 1.5% – 61 % at 25 ºC.

The dry value of the reference gas was determined by sampling the cylinder air without the Swagelok compartment. The LI-7810 reported a water vapour concentration of 0.004 % and a CH_4 concentration of 81.7 ppm. We quantified the influence of water vapour on CH_4 measurements using the method of Chen et al. (2010). A linear relationship was established between: (1) the ratio of wet-air CH_4 concentration (Axetris) to dry-air CH_4 concentrations (LI-7810) and (2) water vapour concentration, as follows:

$$\frac{CH_{4wet}}{CH_{4dry}} = 1 + aH_2O$$

with a = –0.013 ± 0.00008%$^{-1}$. Figure C2 in the Appendix depicts the linear regression.

As mentioned, water vapour affects the measurements in two different ways (Chen et al., 2010). At 81.7 ppm CH_4, this relationship corrects mainly for the water vapour dilution effect, although other effects, including spectral interference and H_2O calibration, account for ~30% of the dilution effect. For field applications, we correct ambient air sample measurements using the derived correction function to convert the measurements in humid air to dry air mole fractions. In practice, water vapour concentrations were either measured directly or taken from model simulations. With this, we assume that the non-dilution part of the water vapour correction remains the same at ambient levels as at high concentrations. Although this approach may not capture the full variability of water vapour, it is expected to adequately account for the most significant sources of water vapour related variability in the measurements. Any residual error introduced by this simplification is considered negligible, especially when compared to larger sources of uncertainty, such as wind variability.

2.5 System precision

The system's precision can be determined by operating it under stable conditions while sampling a reference gas over a longer period. The obtained time series was further analysed using the Allan variance method. The method is a commonly used statistical tool for assessing frequency stability and identifying noise characteristics in measurement systems (Allan, 1966). It provides insight into the noise, stability, and drift of a sensor (e.g., the Axetris), helping distinguish between random noise and systematic drift and informing the user about the optimal calibration frequency. In addition to the stable laboratory test, the sensor was deployed underneath an UAV while it sampled a reference gas from a calibration bag. These tests gave insight into the sensor's precision under more turbulent conditions. The calibration bag used is a ~1 L multilayer gas sampling bag (Supelco Inc.) that was tested and used by Hooghiem et al. (2018) for high-precision stratospheric measurements of CO_2, CH_4, and CO.

The laboratory test lasted for 16 hours, with an observed temperature of 25 ± 0.1 °C and a pressure of 1.02 ± 0.001 bar, while pushing gas through the Axetris at a flow rate of 70 sccm. The UAV's precision was determined over three consecutive flights, each lasting 20 minutes and varying flight patterns. Results were processed in MATLAB using the `allanvar` function (version R2019a), which yielded the Allan variance ($\sigma(\tau)^2$) and the corresponding averaging time (τ). To aid with the interpretability of the resulting figures, we converted the Allan variance to the Allan deviation (in ppb; $\sqrt{\sigma(\tau)^2}$).

Figure 2 shows the Allan deviation results obtained under stable laboratory conditions (16-hour dataset) and during in-flight operation. Figure 2a shows the recorded CH_4 measurements during the 16-hour test and depicts a slow drift in the initial hours of the observations. After being turned on, the system stabilises its cell temperature during the warm-up period. However, the observed drift cannot be linked to this phase, as the system had been on for several hours before the experiment.

https://doi.org/10.5194/egusphere-2025-6209
Preprint. Discussion started: 21 January 2026

Figure 2d shows a precision of 63 ppb at 1-second averaging, improving to 4 ppb at 512-second averaging under stable laboratory conditions. Beyond this duration, the sensor's precision becomes drift-dominated. To maintain measurement precision below 10 ppb, calibration every hour is required. However, when operating the sensor during UAV deployment, its precision decreases. Its performance under flight conditions may differ due to additional pressure and temperature variations, as well as vibrations. In comparison, the Allan deviation analysis of in-flight data (sampled from a calibration bag) shows the sensor's precision of 91 ppb at a 1-second interval, reaching a minimum of 11 ppb after 128 seconds. These results demonstrate the sensor's performance without additional temperature control and show that turbulent conditions reduce its precision.

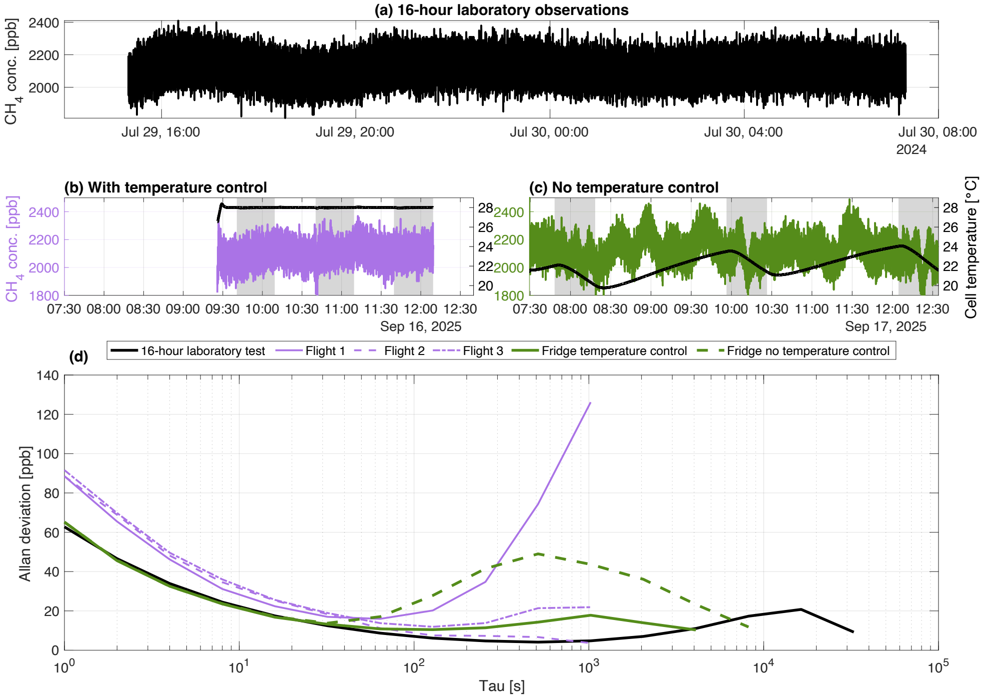

Figure 2: Overview of sensor observations and Allan deviation results. (a) Axetris measurements over sixteen hours during stable laboratory conditions. (b) Axetris measurements (purple) with active temperature control and corresponding cell temperature (black). (c) Axetris measurements (green) without active temperature control and corresponding cell temperature (black). Shaded areas indicate 30-minute periods inside the fridge. (d) Allan deviation plots of the stable laboratory measurements (black), during flight conditions (purple), and with (green) and without (dashed green) temperature control.

2.6 Temperature dependency

Temperature variability is readily observed to affect sensor performance significantly. During routine use, this may lead to biases whenever ambient conditions change, for instance, when moving the sensor from a car to an UAV. To demonstrate this effect and the efficacy of a temperature control system, we conducted controlled experiments. Here, the Axetris was exposed to sudden temperature changes while continuously sampling a reference gas. The conditions encountered during UAV deployment were simulated by transferring the sensor from a room-temperature environment to a fridge (7.5ºC). Airflow around the sensor package (i.e., all components inside a foam casing) was mimicked by placing a small fan inside the fridge. In the experiment, we compared (1) actively heating of the sensor to 28 °C using the heating wire to (2) not heating, and only relying on the dampening effect of the foam casing to provide temperature stability. The Axetris' output was continuously monitored, and the sensor was only transferred after readings had stabilised for ~10 minutes. Each configuration was tested in three independent runs, with the sensor exposed to the cooler environment for 30 minutes per run.

Figure 2b and 2c show the time series of the temperature-dependence experiment, illustrating the necessity of active cell temperature control for stable Axetris measurements under varying ambient conditions. During the experiment, the fridge temperature was 7.6 ± 0.5 °C and the laboratory temperature was 21.4 ± 0.5 °C. Figure 2b depicts the Axetris observations with the cell temperature actively controlled at 28 °C. In contrast, Figure 2c presents the measurements without active temperature control, where irregular and non-linear behaviour is observed. In both panels, the shaded areas indicate the 30-minute periods during which the sensor was placed inside the fridge.

Figure 2d shows the Allan deviation plots for the periods when the Axetris was inside the fridge. As expected, the three tests with active temperature control (green solid line) exhibit decreasing Allan deviations, reaching a minimum of 6 ppb at $\tau = 256\ s$, and stays below ±18 ppb for the duration of the experiment. This is similar to the behaviour observed during the laboratory condition test (black solid line). Without temperature control (green dashed lines), the Allan deviation initially follows the same downward trend. However, it reaches its minimum of 13 ppb at $\tau = 64\ s$. Longer averaging times causes the drift to rise sharply, rising to approximately ±50 ppb.

Active temperature control improves sensor stability and extends the averaging time over which the lowest precision is achieved. In addition, the heating element effectively suppresses the random oscillations observed without temperature control. The random oscillations are detrimental to the system's performance and are too complex to correct. Therefore, observations made when the sensor behaves in this way cannot be used for accurate flux estimation. Finally, in the absence of temperature control, the sensor's stabilisation period after exposure to the colder environment is substantially longer (~100 minutes; Figure 2c), whereas with active temperature control, the sensor is immediately ready for deployment, improving its practicality.

3 Field validation of the Axetris sensor

The laboratory characterisations improved the sensor's observation quality and optimised its performance for in-field deployment. These improvements were then tested during a field validation of the Axetris sensor, comparing its performance with that of the proven Active AirCore technique (Andersen et al. 2018; Morales et al., 2022; Vinković et al., 2022). Both instruments were deployed underneath a UAV during flights at a dairy farm in the north of the Netherlands. These tests allowed for a direct comparison of the two systems for quantifying CH_4 emissions from the whole farm.

3.1 Field site

The dairy cow farm quantified during this study is located in the village of Grijpskerk, approximately 20 km north-west of the city of Groningen. Pastures and cropland surround the farm, with clear upwind areas, making it an ideal location for UAV-based quantification. The farm was previously quantified by Vinković et al. (2022), allowing for direct comparison of our results with theirs. During this study, three main CH_4 sources were identified: a barn with all dairy cows (225 cows), a barn with other cattle (25 dry cows and 132 heifers) and three manure cellars. These sources were also of interest during the study by Vinković et al. (2022).

3.2 UAV system

The sensor package was mounted underneath a DJI Matrice 600 hexacopter UAV using two straps. The UAV has a maximum payload capacity of 6 kg, well above the Axetris package's weight, and a wind speed resistance of 8 m/s. The typical flight duration decreased from 35 minutes (unloaded) to 20-25 minutes when carrying the Axetris package and further decreased when the active AirCore was flown simultaneously. An anemometer (LI-550 TriSonica, LI-COR Biosciences, Lincoln, USA) was mounted on a 1 m tall carbon fibre rod extending from the UAV to obtain in-flight wind speed and wind direction measurements.

3.3 Meteorological measurements

Meteorological data were obtained from both ground-based and drone-mounted sensors, including: (1) a 3D sonic anemometer (WindMaster Pro; Gill Instruments, Hampshire, UK) placed near the farm, which recorded continuous wind speed and direction at 10 Hz at an altitude of 3 meters, and (2) the UAV's onboard wind sensor, i.e. the TriSonica, which provided complementary in-flight measurements. The WindMaster Pro observations were used to anchor a logarithmic wind profile based on the theoretical formulation of Stull (1988).

$$u(z_i) = u_{ref} \frac{\ln\left(\frac{z_i}{z_0}\right)}{\ln\left(\frac{z_{ref}}{z_0}\right)} \tag{1}$$

Equation 1 assumes neutral atmospheric stability and a homogenous surface. A surface roughness length $z_0 = 0.15\ m$ was used, which is representative of conditions between low and tall agricultural crops (Wieringa, 1992). The reference wind speed u_{ref} was derived as the average the WindMaster Pro observations during the duration of each of the flights (Table 1), and z_{ref} denotes the height of these reference observations ($z_{ref} = 3m$), and z_i includes the considered heights. This logarithmic wind profile is used for calculation of fluxes.

To visually assess the appropriateness of the logarithmic profile, we plot it together with the TriSonica measurements and observations from the two nearby Royal Netherlands Meteorological Institute (KNMI) stations (Appendix D). Raw TriSonica measurements were converted to true wind speed and direction by accounting for the UAV's motion and orientation. Overall, the TriSonica observations show a clear increase in wind speed with altitude, resembling the cardinal feature of the logarithmic profile. The uncertainty bounds of the TriSonica data overlap with the profile, indicating that our assumptions about the logarithmic profile are reasonable under the flight conditions. In addition, observations (reported as u_{10}) from the KNMI stations at Eelde (~ 30 km SE from the farm) and Leeuwarden (~ 25 km W) were included in Appendix D. The TriSonica observations corroborate the existence of a logarithmic profile, warranting its use over that of a single wind speed value over the full altitude range.

3.4 Active AirCore

The active AirCore system provides semi-continuous sampling and analysis of various trace gases. In this study, we measured CH_4 mole fractions along flight trajectories using an upgraded version of the system described by Andersen et al. (2018). The AirCore consists of a 95 m stainless steel coil (635 mL volume) that samples ambient air at a controlled flow rate of ~ 23 sccm, allowing approximately 27 minutes of flight time. However, due to the UAVs battery and the total payload, the maximum flight duration was only 15 minutes. After landing, the AirCore was connected to the LI-7810 to measure the CH_4 mole fractions from the collected air samples. The samples were pulled through the AirCore and into the analyser and followed by one of the two available gas mixtures from cylinders. Alternating, per flight, between the two gas tanks enabled easy identification of the start and end points of the analysis. In this manner, two flights per hour can be achieved.

A primary challenge of the active AirCore technique is assigning the CH_4 concentration readings from the gas analyser (LI-7180) to the flight trajectory. In principle, simultaneous flights with the Axetris and the AirCore allow for improved alignment, as in situ observations permit direct temporal and geospatial projection of AirCore measurements. This method was indeed implemented here but did not appreciably improve the results of the nominal mapping, shifting the assigned timestamps of the project AirCore data by less than 2 seconds (i.e., ~5 meters horizontal).

3.5 Flight strategy

The UAV equipped with both sensor packages was flown downwind of the dairy farm at a constant speed of 3 ± 0.5 m/s while maintaining stable orientation and with the sampling inlet pointed into the wind. The UAV flight track was oriented approximately perpendicular to the wind direction to achieve optimal cross-sectional sampling. A wireless connection enabled the ground team to monitor CH_4 concentrations in real time and ensure sufficient sampling outside the plume, which is essential for obtaining sufficient background data and properly constraining the extent of the plume. Continuous sampling was conducted along transects at multiple altitudes, typically at 5 m vertical intervals. The maximum altitude ranged from 40 m to 70 m, depending on plume height.

A total of five UAV flights were performed on the 29th of July 2025, with flight duration ranging from 11 to 17 minutes, depending on battery capacity, meteorological conditions, and payload mass. Weather conditions were cloudy, with occasional rain and temperatures ranging from 18 °C to 21 °C. Typical wind speed was 4 m/s (maximum 8.5 m/s) at 3 m above ground level (Appendix D). Table 1 provides a complete overview of the flight characteristics.

Table 1: Summary of the five downwind flights conducted on 29 July 2025.

29 July 2025

https://doi.org/10.5194/egusphere-2025-6209
Preprint. Discussion started: 21 January 2026

Flight time [min]	13	16	11	16	17
Take off [hh:mm:ss] [UTC]	11:45:18	12:22:35	13:14:08	13:51:30	14:31:28
Landing [hh:mm:ss] [UTC]	11:58:52	12:38:28	13:25:05	14:07:32	14:48:26
Mean UAV speed [m/s]	2.9	3.0	3.4	3.0	2.9
Mean wind speed [m/s] *	2.3 ± 0.5	3.9 ± 0.8	4.5 ± 0.8	4.0 ± 1.0	2.5 ± 0.8
Mean wind direction [°]*	290 ± 14	309 ± 9	319 ± 10	302 ± 14	277 ± 17
Flux estimate Axetris [gCH₄/s]	2.8	5.5	-0.1†	5.4	2.8
Flux estimate AirCore [gCH₄/s]	3.2	5.2	4.4†	5.0	3.0

* The wind direction and speed are obtained from the 3D sonic anemometer and observed at a height of 3 meters

† Temperature control failed during flight 3, this flight will be excluded from further analysis

3.6 Spatial interpolation

Spatial interpolation is crucial for estimating CH_4 mole fractions at unsampled locations, which are subsequently used to calculate the total emission flux. In this study, observed CH_4 enhancements were interpolated onto a grid using a Gaussian weighting scheme with finite spatial influence. This approach produces smoother concentration fields than alternative techniques such as inverse distance weighting (Di Piazza et al., 2011), because the Gaussian kernel gradually reduces the influence of distant measurement points rather than abruptly discarding their contributions. The weight assigned to each observation is computed as:

$$\omega_j = \exp\left(-\left[\left(\frac{x_i - x_j}{r_{inf}^x}\right)^2 + \left(\frac{y_i - y_j}{r_{inf}^y}\right)^2\right]\right) \tag{2}$$

where (x_j, y_j) are the coordinates of the observations, (x_i, y_i) are the location of the grid cell, and r_{inf}^x, r_{inf}^y are the influence radii in the vertical and horizontal direction, respectively. Furthermore, observations outside a predefined cutoff radius are excluded from the interpolation, effectively spatially limiting the influence of each observation. This limit is required because the Gaussian kernel gradually reduces in strength but never reaches zero.

The estimated CH_4 mole fraction, c_i, at each grid location is then computed as a weighted average using:

$$c_i = \frac{\sum_{j=1}^{\mathcal{N}_i} \omega_j z_j}{\sum_{j=1}^{\mathcal{N}_i} \omega_j} \tag{3}$$

where z_j is the observed value and $\mathcal{N}_i$ is the set of observations that fall within the cutoff radius of grid points i. Grid cells with no contributing observations (i.e., beyond the cutoff radius of the nearest measurement) are assigned missing values (`NaN`) and excluded from subsequent analysis.

3.7 Mass balance

The spatially interpolated CH_4 concentrations were used to estimate the farm's total CH_4 emission rate by implementing the results in the mass balance approach (MBA) similar to Nathan et al. (2015) and Vinković et al. (2022). The following equation gives the MBA:

$$Q_{CH4} = \cos(\theta) \frac{M_{CH4}}{M_{vol}} F_{ppb} \sum_{i=1}^{N_z} \sum_{j=1}^{N_x} \Delta x \Delta z \Delta c_{i,j} u_{prof}(z_i) \tag{4}$$

where u_{prof} is the logarithmic wind profile (in m/s, as described in Eq. 1), θ the angle between the mean wind direction and the direction perpendicular to the flight track, Δx and Δz represent the horizontal and vertical grid size of the integration plane, the molar mass of methane is given by M_{CH4}, Δc gives the CH_4 mole fraction enhancement above the background in ppb, F_{ppb} is the unitless conversion factor from ppb to mole fraction and M_{vol} gives the molar volume and is defined as:

$$M_{vol} = \frac{RT}{P(1-H_2O)} \tag{5}$$

where R is the universal gas constant, T is the ambient temperature in Kelvin, P is the ambient pressure in Pascal, and H_2O is the mole fraction of water vapour in the air. In this work, the ambient H_2O mole fractions were obtained using the LI-7810 analyser. If in-field observations of [H_2O] are not possible, a mean value may be approximated from RH% observations from nearby meteorological stations. All other meteorological parameters were recorded during flight and used to calculate the CH_4 flux Q_{CH4} through the integrated plane. The obtained flux is interpreted to equal the emission at the farm. The resulting emission estimates are reported in grams per second (g s^{-1}).

As stated, Δc represents the CH_4 mole fraction enhancement above background. For the AirCore, the background concentration was determined as the 10th percentile of the observations, under the assumption that the UAV sampled beyond the plume boundaries. The 10th percentile method is not suitable for the Axetris due to its higher noise level. This method would result in an overestimated flux, as it selects only the lowest observations from the Axetris.

Rather for the Axetris, the background was defined as the mean CH_4 mole fraction from the measurements obtained outside the plume boundaries. To identify these regions, CH_4 concentrations were plotted against the horizontal distance travelled, and the area with the lowest values was selected based on visual inspection and all observations in the area were averaged (Appendix E). Under ideal conditions, this plot reveals a distinct separation between elevated CH_4 values (associated with plume observations) and lower, stable values representing the background. By assuming that the lower CH_4 observations correspond to the background and including a large number of data points, the estimated background value is expected to closely approximate the true atmospheric background and to have a low uncertainty.

The averaging background method is not ideal for the Active AirCore due to its intrinsic signal smoothing (Morales et al., 2022). To use the same method, longer sampling outside of the plume should be part of the flight strategy (Appendix E), limiting the collection of plume samples. The AirCore and Axetris methods report different backgrounds, since both instruments were only approximately calibrated during the field campaign. Flux quantifications for each sensor are conducted with its respective technique and background concentration.

3.8 Comparison of results of Axetris and AirCore

An illustrative overview of the second of the five UAV flights is shown in Figure 3. The top panel (Figure 3a) shows the raw Axetris observations (black), the smoothed Axetris (green) and the AirCore observations (purple). All measurement series clearly show repeated detection of the CH_4 plume.

The smoothed Axetris measurement series is plotted merely for illustrating the likeliness between the results of the two instruments. It was obtained using *locally weighted scatterplot smoothing* (LOWESS) of the raw signal; a window size of 50 samples gives an overall best resemblance to the AirCore data; the integral of raw and smoothed Axetris data is identical. The projected AirCore measurements are well aligned with the in situ sensor data, demonstrating the accuracy of the projection methodology. Moreover, regression between the smoothed Axetris data (using the LOWESS), and the AirCore data yields a correlation coefficient of 0.92 (Appendix F), with a mean difference of 89 ± 39 ppb (1σ) over all flights. This mean difference may be attributed to the improper calibration of the sensors which is supported by the significantly reduced difference of 26 ± 44 ppb (1σ; over all flights) between the CH_4 enhancements (i.e., after removal of the background). The large standard deviation may be attributed to (1) the differences in response time, as the LOWESS for the Axetris is only approximate to the Taylor and molecular dispersion that appears in the AirCore and the additional smearing effect inside the measurement cell of the LI-7810 (Andersen et al., 2018) and (2) A slight temporal shift between the two signals that cannot be completed eliminated also contributes to the difference. We use the raw signal in subsequent analysis.

Figure panels 3b and 3c show the spatially interpolated Axetris and Active AirCore data, respectively. The AirCore method produces a wide and smooth plume compared to the narrow and more sharply enhanced plume derived from the Axetris data (Figure 3b). The results of these interpolations were used with the MB equation (Eq. 4) and the logarithmic wind profile (inferred from the WindMaster Pro data) to calculate the full farm emission flux, reported in Table 1. The emissions estimates derived by the two methods (AirCore, Axetris) differed by less than 10%, both for individual flights as for the mean of flights.

The flights were conducted under light to moderate wind conditions (3.7 ± 1.4 m/s, NW to WNW; Appendix D) and consisted of 12 transects between 4 and 60 m above ground level at approximately 120 m downwind of the farm (Appendix G). This variability in wind speed and direction can influence the flux estimate, leading to an over- or underestimation of the emission (Mohammadloo et al., 2025). A change in wind direction can cause the plume centre to shift, increasing the probability of sampling the full plume multiple times during flight or missing it altogether. Performing multiple passes across different altitudes, these plume-displacements can be captured and accounted for in the final flux estimate. Variability in the wind speed alters both the plume advection and dispersion. Higher wind speeds tend to elongate the plume and dilute observed concentrations, whereas lower wind speeds have the opposite effect (Stull, 1988).

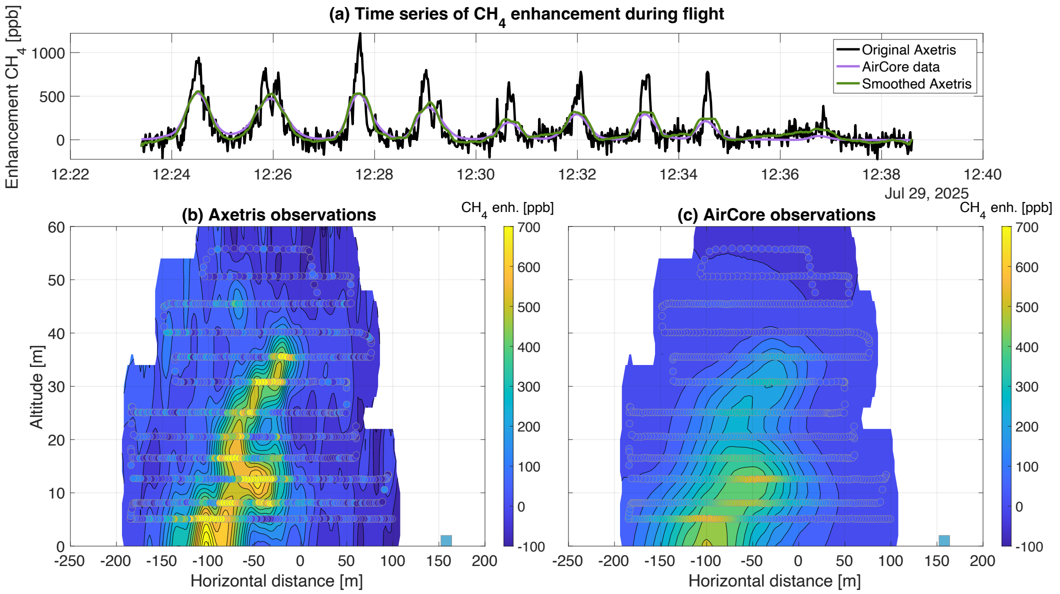

Figure 3: observations and the spatially interpolated data from the second flight conducted on 29 July 2025. The middle of the barn is at 0m horizontal distance, and the blue square shows the take-off location. (not in-plane). (a) shows the measurement series of CH_4 enhancements of the AirCore (purple; projected onto the Axetris flight times), the raw Axetris data (black), and smoothed Axetris data (green). (b) shows the spatial interpolation of the raw Axetris data. (c) shows the spatial interpolation of the AirCore data.

The emission rates of the farm estimated from individual flights ranged from 3.5 to 5.2 gCH_4/s for the AirCore method and from 2.8 to 5.5 gCH_4/s for the Axetris method (Appendix H). Flight 3 was excluded from the analysis due to a failure in the active temperature control, causing the Axetris sensor to drift and rendering the observations invalid. The subsequent analysis is based on four of the five flights. The average emission rate across all quantifications using the active AirCore is 4.2 ± 1.1 gCH_4/s (1σ; n=4). The Axetris yielded a similar value of 4.1 ± 1.6 gCH_4/s (1σ; n=4), when using their respective background concentrations. When averaging all four flights, the flux estimates and the standard deviation between them are similar, indicating that the Axetris can determine flux comparably to a high-precision sensor. The correlation between the individual flight observations is strong: whenever the Axetris observed high fluxes, so did the active AirCore (Table 1). This consistency indicates that both instruments respond similarly to external stochastic influences (e.g. wind uncertainty and emission variability), rather than measurement-concentration issues. This shows that the two independent systems are capable to capture the same underlying atmospheric signal, strengthening the functionality of a cost-effective sensor for emission flux quantification.

The reported uncertainty ranges represent the mean and standard deviation (1σ) of the fluxes obtained from the four flights. Consequently, the standard deviation presented depicts the variability among the nominal flux determinations rather than the underlying measurement uncertainties. However, each flux has its own uncertainty, arising from variations in meteorological conditions, sensor performance and background determination. Quantifying the exact uncertainty associated with these sources can be labour-intensive yet is essential for accurately assessing the robustness of the results. To address the uncertainty associated with each source, a statistical analysis was performed to assess the individual and combined effects of each source, as described in following section.

The flux estimates obtained in this study were higher than those reported by Vinković et al. (2022), who observed values between 1.1 and 2.5 gCH$_4$/s at the same farm. Although not directly relevant to our instrument development, the discrepancy warrants brief discussion. A plausible explanation for this discrepancy can be the timing of our flight measurements. Our campaign was conducted during the summer months, when higher ambient temperatures coincided with enhanced animal activity and enhanced microbial activity in the manure (Vechi et al., 2023; Vinković et al., 2022). In addition, active emptying of the manure storage was taking place during the flights. Such management activities can provoke short-term emission spikes, as agitation and pumping of liquid manure can release trapped CH$_4$ (Leytem et al., 2017; Vanderzaag et al., 2010), which may explain the higher flux. Finally, unlike Vinković et al. (2022), who assumed a constant wind speed for the MBA, our analysis used a logarithmic wind profile that accounts for increasing wind speeds at higher altitudes (Appendix D). This leads to larger flux estimates, since the concentration enhancements at higher altitudes are multiplied by wind speeds that exceed the 3-m reference value (3D-sonic).

4 Statistical analysis

4.1 Simulated plume sampling

To assess the robustness and uncertainty of our UAV-based emission quantification efforts, a statistical model was developed broadly following the approach of Mohammadloo et al. (2025). The model is based on the Ornstein-Uhlenbeck (OU; Uhlenbeck & Ornstein, 1930) process, which is well-suited for modelling events that fluctuate around a long-term mean. It combines random walk tendency (i.e. Brownian motion) with a mean-reverting process of which the restoring force is proportional to the deviation magnitude. Over time, this results in a normally distributed variation around the mean. The incremental evolution of a variable (χ) governed by the OU process is given by:

$$d\chi_t = \theta\big(\chi_0 - \chi(t)\big)dt + \sigma\chi dW_t \tag{6}$$

where χ is the time-varying variable of interest, χ_0 is its initial value, θ is the mean-reverting term, $\sigma\chi$ is the diffusion coefficient representing process noise and dW_t is an increment of the standard Wiener process.

We used the model to generate a time-varying CH$_4$ plume under dynamic atmospheric conditions, represented as a two-dimensional Gaussian distribution on a two-dimensional plane, whose extent, vertical and horizontal position and intensity oscillate around long-term means (Appendix I). This simulated plume may be sampled at the locations and times of a simulated or actual drone flight. We subjectively tune the model parameters to yield

https://doi.org/10.5194/egusphere-2025-6209
Preprint. Discussion started: 21 January 2026

results that closely resemble our real-world findings, after synthetic sampling and processing similar to section 3.6 and 3.7.

The OU approach allows for computationally efficient approximation of certain aspects of turbulent variability. However, it clearly does not replicate the full spatial complexity of plume dynamics. In contrast, large eddy simulation (LES; Dosio & de Arrelano, 2006; Ražnjević et al., 2022) provides the full 4D behaviour of plumes, comprehensively including multiple turbulent features including filaments, large eddies and vertical mixing, albeit at much greater computational expense.

4.2 Uncertainty analysis

Systematic and random uncertainties in UAV-based flux measurements are challenging to quantify directly in the field. Monte Carlo (MC) simulations provide a practical means to approximate them. In this study, we used the OU-based model to generate a three-hour artificial plume with a mean emission rate of 10 kgCH₄ hr⁻¹ (i.e., 2.78 gCH₄ s⁻¹). Realistic plume cross-sections samplings were simulated by using a typical flight trajectory from the previous field campaign (specifically flight 1; Table 1). This trajectory was used to repeatedly (N=500) sample synthetic plume data. Each run was made unique by randomly selecting a different start time within the three-hour plume simulation. This setup formed the basis for evaluating five sources of uncertainties (Table 2). These sources were examined individually, and in combination with each other, in defined *scenarios.* Within each *scenario*, 500 *synthetic plume samplings* and *flux estimations* are performed to ensure statistical robustness while remaining computationally feasible. The resulting flux estimate distributions were analysed to derive the mean bias, standard deviation and 95% confidence intervals (CI; defined as the 5th and 95th percentiles of the distribution of the 500 inferred individual fluxes) associated with each source of uncertainty.

Table 2: Overview of the scenarios considered during this study, the reason behind the interest in the scenario and the method of evaluation.

Scenario	**Reason**	**Method of evaluation**
(1) Flight duration	Longer flights may more representatively sample the plume	Mimic longer flights by repeating the nominal flight path 1 – 6 times. (6x500 samplings)
(2) Background determination	Uncertainty in the background concentration, e.g. from bad initial assessment or gradual sensor drift, affects inferred flux	Deviate background concentration with a random variation of ±0, ±5, ±10, ±15, ±20, ±30, ±40 and ± 50 ppb (8x500 samplings)
(3) Wind speed	Flux estimates in the MBA scale linearly with wind speed, any under- or overestimation of (average) wind speed directly leads to a bias in the calculated flux	Addition of uncertainty in wind speed determination from 0% to 50%, with steps of 5%; constrain wind speed ≥ 0 m/s (11x500 samplings)
(4) Sensor noise	Higher noise levels reduce the detectability of small enhancements	Vary instrumental noise during synthetic sampling, with variations between 5 and 150 ppb (12x500 samplings)

(5) Combined uncertainty	Quantify expected uncertainty of one flight during field deployment	Simultaneously include all individual uncertainty contributors, assuming: (1) a background uncertainty of 10 ppb; (2) wind speed variability of 20%; (3) a sensor noise level of 62 ppb. (1x3000).

Table 2 lists the uncertainty contributors considered during this study, and the evaluation method in our OU-model. This uncertainty analysis allowed for a systematic evaluation of how individual and combined uncertainty sources propagate into UAV-based flux estimates, revealing the relative influence of each contributor. The setup for scenario 5 is based on parameter estimates from field campaigns and observations.

4.2.1 Flight duration

Figure 4a shows how the standard deviation between the 500 modelled flights decreases with increasing duration of each flight. As expected, the results indicate that uncertainty decreases with longer (or repeated) flights, increasing the probability of representatively quantifying the full plume. With only a single flight (~12 minutes), the mean flux is 10.3 kgCH_4/hr [5.5–16.7 kgCH_4/hr; 95% CI]. Increasing the flight duration lowers the CI bounds and the standard deviation, with the standard deviation decreasing from 27% (1σ) for one flight to 15% for three flights [7.5–13.6 kgCH_4/hr] and reaching its minimum of 11% for six flights [8.4–12.7 kgCH_4/hr].

Increased flight duration decreases the CI of the flux estimates, as depicted in Figure 4a. One flight per source increases the possibility of reporting an over- or under-representation of the total flux. With short flights (or a low number of flight repeats), atmospheric stochasticity has a larger impact. Increasing the number of flight repeats and averaging the resulting estimates offset this concern. With more flight repeats, flights are conducted across a wide range of conditions, increasing the likelihood of representatively quantifying the plume.

4.2.2 Uncertainty effects of background errors

As mentioned in section 3.7, multiple techniques are available to determine the in-flight background concentrations. However, the assumptions underlying these techniques, e.g. spatial and temporal uniformity of the background, instrument precision and absence of drift or sufficient sampling outside the plume, may not always hold (Edwards et al., 2025). This introduces an additional source of uncertainty into flux measurements. Reliable background determination is essential for accurate flux quantification, as even minor discrepancies can introduce systematic errors and consequently bias flux estimates (Allen et al., 2019; Cambaliza et al., 2014).

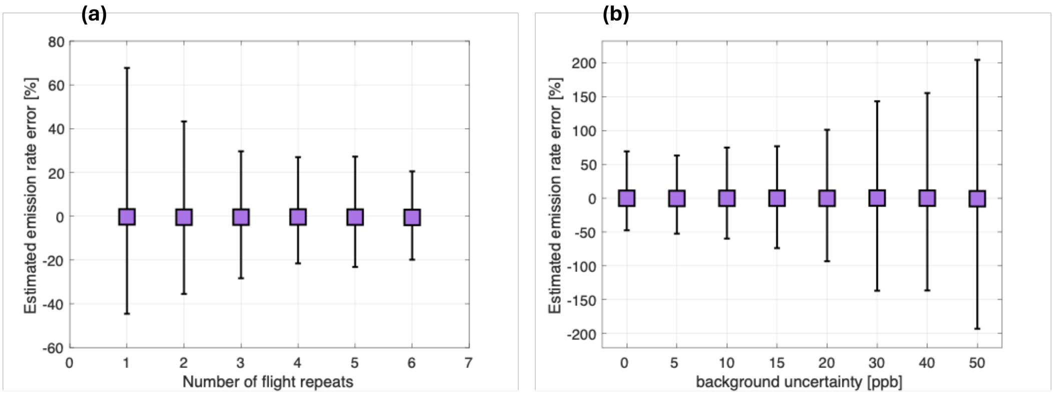

Figure 4: The marker shows the mean error, and the error bars present the 95% confidence interval. (a) An overview of the emission flux estimates and the variability from 500 repeat simulations with an increase in flight repeats. (b) An *overview of the uncertainties linked to the background determination.*

Figure 4b shows the impact of the uncertainty in the background determination on the flux estimate. Each run calculated the flux using the MBA with a varying background concentration. The figure shows that the estimated emission error increases with increasing background uncertainty. A background uncertainty of 30 ppb results in an estimated flux of 10.2 kgCH_4/hr ([-3.6–23.9 kgCH_4/hr; 95% CI]), and a standard deviation of 70% (1σ). Based on the standard error of the observed background in our flights, we expect to be able to determine background concentrations with an uncertainty of ±10 ppb. Assuming the uncertainty in the background to 0–10 ppb, constrains the standard deviation to below 35% (1σ). However, we infer a high sensitivity of the inferred flux to errors in the assumed background. At ±20 ppb uncertainty in the background the standard deviation exceeds 100%, i.e., yielding a negative or double flux, underscoring the importance of accurate background concentration determinations.

4.2.3 Wind speed uncertainty

Wind speed uncertainties are known to introduce significant errors into flux estimates (Allen et al., 2019; Morales et al., 2022; Vinković et al., 2022). Figure 5 shows an overview of the simulation results for varying wind speeds (Figure 5a) and instrumental noise (Figure 5b).

Uncertainties in the wind speed profiles were generated by multiplying the expected logarithmic profile by its respective uncertainty, yielding unique wind profiles for each Monte Carlo realization, thus representing the situation where the true mean windspeed is different from what is assumed in subsequent calculations. Figure 5a shows the outcome of this analysis and the contribution of wind speed uncertainties to the overall emission flux errors. A low wind speed uncertainties (<10%) limits the standard deviation to 30% (1σ), and results in a flux estimate of 10.1 kgCH_4/hr [5.0, 17.1 kgCH_4/hr; 95% CI]. However, when the uncertainty increases, so does the standard deviation and the flux estimate. With a wind speed uncertainty of 50%, the standard deviation of the determined flux exceeds 60% (1σ), and the flux estimate becomes 9.7 kgCH_4/hr [0.6–23.7 kgCH_4/hr; 95% CI].

These findings highlight the importance of minimising the wind speed errors by obtaining reliable wind speed measurements during flights.

The results, showing an increase in the flux uncertainty with greater wind speed uncertainty, was expected. However, the finding contradicts Mohammadloo et al. (2025), who reported that flux estimates are unaffected by wind-speed variations because measured concentrations scale proportionally with wind speed. In principle, this is correct, since for a constant source strength, higher winds yield lower concentrations. Errors in assumed wind speed may stem from to changing atmospheric conditions and can lead to the calculation of the emission flux using an incorrect wind speed, whilst the concentrations remain the same.

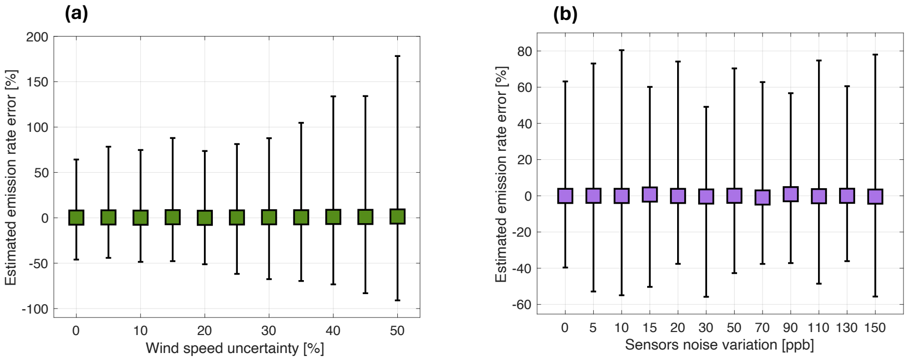

Figure 5: The marker shows the mean error, and the error bars present the 95% confidence interval. (a) An overview of the emission flux estimates and the effect of the wind speed uncertainty (b) An overview of the uncertainties linked to the instrumental noise.

4.2.4 Uncertainty effects of instrumental noise

High-frequency sensor noise makes it hard to accurate resolve brief spikes in CH_4, for instance during high-speed flights. To an extent this may be alleviated by reducing flight speed, at the expense of reducing plume coverage (for a given UAV endurance). Low-noise sensors thus in principle allow for improved detection of smaller plumes or improved spatial resolution the nominal plume. Here, we mimic the effect of noise in the Monte Carlo simulation, applied by varying the noise levels added to the trace (time series) sampled from the simulated plume. The sensor's noise (at 2 Hz) was varied from 5 to 150 ppb, generically representing high-, to low-precision sensors. Figure 5b shows that increasing noise does not directly affect the estimated error, as random fluctuations largely cancel during spatial interpolation.

The main impact of changing sensor noise is on background determinations. High-precision sensors usually allow straightforward application of approaches such as the 10th percentile method, whereas higher-noise sensors require additional processing with typically less certain results. Without this processing, applying the 10th percentile method to noisier sensors will lead to an overestimation of the flux, since the enhancements will appear larger than they actually are.

4.2.5 Combined uncertainty

The individual uncertainty analyses provide valuable insights into the role of individual factors on the emission estimate. During field campaigns, these factors (among others) are expected to affect the flux quantification simultaneously. To assess their combined effect, all the above sources of uncertainty were analysed in a single MC simulation. These uncertainty contributors were set to values (Table 2.) encountered during actual deployment.

This simulation was used to estimate the overall combined uncertainty during our field campaign for a single flight. With the above-mentioned setup, the obtained flux was 10.0 kgCH_4/hr ([3.3–19.1 kgCH_4/hr; 95% CI), with a standard deviation of ± 40% (1σ). The uncertainties reported are consistent with those from previous studies (Andersen et al., 2021; Karion et al., 2013; Morales et al., 2022; Nathan et al., 2015).

4.2.6 Summary

This statistical analysis covered a range of potential sources of uncertainty to elucidate their expected contribution to the emission flux estimates. Table 3 provides an overview of the uncertainty sources discussed and their effects on the standard deviation, from the nominal scenario to the most considerable impact. Table 3 highlights that the background uncertainty and the wind speed uncertainty have the highest impact on the uncertainty of the estimate of the flux. Sensor noise is determined to not be a meaningful factor, especially when other uncertainties are more substantial (depicted in Table 3).

Table 3: Summary of the influence of various sources of uncertainty

Scenario	**Uncertainty ranges considered**	**Effect on (1σ)**
Flight duration	1 → 6 repeats	27% → 11%
Noise	0 ppb → 150 ppb	27% → 28%
Background	0 ppb → 50 ppb	27% → 100%
Wind speed	0% → 50%	27% → 62%
Combined uncertainty	Everything 0 → Set uncertainties	27% → 40%

4.3 Applicability to various source strengths

During the uncertainty analysis, the influence of individual sources was evaluated for a reference emission rate of 10 kgCH_4/hr. In practice, emission rates can vary widely depending on source type and environmental conditions, and the relative importance of different uncertainty sources depends strongly on the source strength. Most importantly, the background uncertainty and sensors noise may become too large to derive a meaningful flux. To assess this relationship, we repeated the analysis in 4.2.5 for source strengths ranging from 1 to 20 kgCH_4/hr and performing 1-6 flight repeats using 500 MC realizations each. The results are summarized in Figure 6.

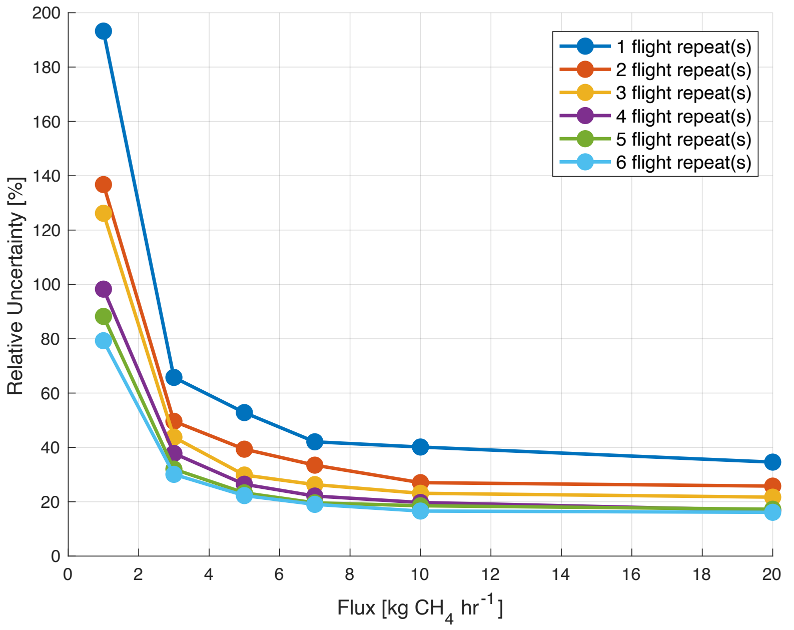

Figure 6: Relative uncertainty in flux estimates for emission rates of 1-20 kgCH$_4$/hr across a range of flight repeats.

Figure 6 shows that multiple flight repeats reduce relative uncertainty. At lower emission rates, flux estimates are more susceptible to instrumental errors, where noise and background uncertainties are dominant factors. These random errors are effectively averaged out through repeated sampling. In contrast, estimates of larger emission rates are less influenced by sensor performance and are instead dominated by meteorological errors. As these errors are not reducible through averaging, multiple flight repeats result in a persistent uncertainty of approximately 20% (1σ).

5 Discussion

This study evaluated the performance of a cost-effective CH_4 sensor and demonstrated that it can provide emission flux estimates comparable to those obtained with a higher-precision UAV-based instrument (i.e. Active AirCore). Field validation showed that the cost-effective sensor produced flux estimates that differed <10% from those obtained by the Active AirCore method. Results from the Active AirCore technique have a standard deviation of 26% (1σ), while that of the Axetris exceeds 39% (1σ). This uncertainty is a combination of systematic errors, random errors in wind-related uncertainties, background uncertainties and variability in the actual flux.

The results indicate that, for the assessed farm flux of ~4 gCH$_4$/s, total uncertainty associated with our UAV-based flux estimates is influenced more by uncertainties in wind variability and plume sampling methods than by the precision of the employed mid-cost sensor. With active temperature control, the Axetris sensors uncertainties are similar to those found during prior UAV-based studies (Andersen et al., 2021; Karion et al., 2013; Morales et al., 2022; Nathan et al., 2015) using higher precision and accuracy sensors.

The necessity or low drift is well illustrated by Flight 3, which showed the impact on Axetris CH_4 readings of (strong) cell temperature drift. The drift occurred as a result of faulty PID control: the sensor accidentally warmed prior to flight, and thus cooled during flight, see Figure A2. This clear drift of the measurement baseline, and an apparent oscillation around that (see data at 13:14) hinders the assessment of the background CH_4 and thus to infer a meaningful flux.

This study highlights that improving post-flight data processing and obtaining accurate in situ meteorological observations are most important for reducing UAV-based uncertainties. These findings are consistent with previous studies that identify wind speed and direction as dominant sources of uncertainty in UAV-based CH_4 flux estimation (Morales et al., 2022; Yong et al., 2024; Mohammadloo et al., 2025; Wietzel et al., 2025). Wind-related errors are difficult to mitigate and can propagate non-linearly through the MB calculation, as a combination of wind direction and wind speed uncertainties. Background concentration uncertainty can typically be reduced through sufficient downwind sampling. Especially, small source strengths are influenced by background uncertainty, since the enhancements are usually small. Yong et al. (2024) noted that background variation accounted for only 6% of the total uncertainty, with a strong source. The uncertainty found in this study, showed a larger uncertainty with smaller sources, indicating that sources with considerable enhancements are less influenced by a 10 ppb change in background concentrations.

This study did not include the effects of spatial sampling density, which can also affect the accuracy of the emission flux measurements. Significant data gaps negatively affect the MBA, leading to systematic underestimation of the emission flux. This limitation has been addressed in detail by Mohammadloo et al. (2025). Higher-frequency observations in the horizontal and vertical directions decrease the estimated emission rate error. Based on their findings and our own flight track featuring relatively dense horizontal and vertical coverage, we expect to have only an additional 5-10% error. Future work should combine optimised flight-path design with real-time plume detection to further minimise spatial sampling bias.

Our flight strategy provided abundant sampling with multiple transects at varying altitudes, creating favourable conditions for both IGA and MBA. Andersen et al. (2021) studied fluxes from coal-ventilation shafts using both methods and showed higher uncertainties for the MBA (26-51%), compared to the IGA (8-16%). In their research, the MBA uncertainty is dominated by wind speed. The IGA uncertainty reflects the standard error derived from 1000 optimisation iterations. Kim et al. (2023) also mention that the IGA is less sensitive to undersampling of plumes and upwind background levels, but the method can be considerably influenced by atmospheric stability.

Wind direction during the flights was variable, leading to a horizontally stochastic plume observations, making appropriate the use if a method that does not rely on Gaussian plume assumptions. The analysis from Andersen et al. (2021) underscores the importance of multiple transects at different altitudes, and that the IGA performed best when the vertical spacing and the distance were smaller than 2.5 times the vertical distribution (σ_z) of the plume. Given that our sampling was abundant but accompanied by temporally varying winds, we employed only the

https://doi.org/10.5194/egusphere-2025-6209
Preprint. Discussion started: 21 January 2026

MBA, as it remains valid without requiring a stable Gaussian plume structure and provides a transparent, wind-driven uncertainty estimate.

Overall, the findings highlights that the implementation of cost-effective sensors offers a promising way to expand the spatial and temporal coverage of regional CH_4 monitoring. This scalability can improve emission quantification across a variety of sources, such as landfills, farms and wastewater treatment plants. The study reiterates that to maximise effectiveness, standardised flight procedures are required, together with precise background assessment and accurate meteorological observations during flight.

6 Conclusion

This study demonstrates the possibility of using a cost-effective, medium-precision, in situ CH_4 sensor on UAVs for rapid emission assessment. Laboratory characterisation indicates that temperature fluctuations stongly affect this sensor's measurement stability, rendering it unreliable for this work unless appropriate mitigative measures are taken. We improved the sensor's performance by properly insulating the sensor and applying active thermal regulation to maintain a constant cell temperature (±0.05 °C). Adding active temperature control removes the unwanted measurement oscillations, maintaining the long-term accuracy of the Axetris even when bigger environmental temperature changes are present. Allan variation analysis confirmed that under stable laboratory conditions, the sensor achieves a precision of 63 ppb at 2 Hz and remains stable to within ±10 ppb over a 20-minute time scale. Insights gained from lab characterisation supported the preparation of the sensor for UAV-based field tests. With active temperature control, and observing large temperature differences, the sensor remains stable within ±20 ppb over a 20-minute time scale.

Field experiments at a dairy farm confirmed that the Axetris can deliver reliable CH_4 flux estimates, comparable to those obtained using the established Active AirCore technique. Across four flights, the mean flux derived from the Axetris measurements was 4.1 ± 1.6 gCH_4/s, while the AirCore measurements yielded a flux of 4.2 ± 1.1 gCH_4/s. The close agreement between the techniques validates the use of the Axetris sensor for robust flux quantification.

An uncertainty analysis using the Ornstein-Uhlenbeck approach to identify the dominant sources of uncertainty in UAV-based flux measurements shows the noise of this sensor does not significantly impact the total uncertainty, particularly when emission sources are sufficiently large and plume coverage is sufficient in space and time. In contrast, realistic uncertainties in wind speed estimates (common at low wind speeds) can introduce errors in the flux exceeding 60%. An accurate determination of background concentration is also important, since errors in background estimation can account for more than 100% of the total uncertainty for a flux of 10 $kgCH_4/hr$, with even greater sensitivity when CH_4 enhancements are low. Overall, weaker emission sources are more affected by instrumental errors compared to stronger sources. Multiple flight repeats help to reduce the uncertainty in the background determination and average the effects of variable wind speeds and direction, while systematic errors in the wind speed (e.g., the assumed profile) remain persistent.

This study underscores that careful laboratory testing and compensation for environmental temperature variability, can significantly improve the performance of medium-precision sensors for flux estimation. This supports the potential for deploying these cost-effective sensors on UAV systems for GHG monitoring, thereby helping to close data gaps in national inventories.

Data availability: The data and code used in this study will be provided by the authors upon request.

Acknowledgement. We would like to thank Roland Kooiker for his years of support for our campaigns, and for his willingness to open his farm to our team.

References

Allan, D. W. (1966). Statistics of atomic frequency standards. *Proceedings of the IEEE, 54*(2), 221-230, https://doi.org/10.1109/PROC.1966.4634

Allen, G., Hollingsworth, P., Kabbabe, K., Pitt, J.R., Mead, M.I., Illingworth, S., Roberts, G., Bourn, M., Shallcross, D.E., Percival, C.J. (2019). The development and trial of an unmanned aerial system for the measurement of methane flux from landfill and greenhouse gas emission hotspots. *Waste Manag*. 87, 883–892. https://doi.org/10.1016/j.wasman.2017.12.024.

Andersen, T., Scheeren, H.A., Peters, W., Chen, H. (2018). A UAV-based active AirCore system for measurements of greenhouse gases. *Atmos. Meas. Tech. 11*, p2683-2699. https://doi.org/10.5194/amt-11-2683-2018

Andersen, T., Vinković, K., de Vries, M., Kers, B., Necki, J., Swolkien, J., Roiger, A., Peters, W., & Chen, H. (2021). Quantifying methane emissions from coal mining ventilation shafts using an unmanned aerial vehicle (UAV)-based active AirCore system. *Atmospheric Environment: X*, 12. https://doi.org/10.1016/j.aeaoa.2021.100135

Bousquet, P., Pierangelo, C., Bacour, C., Marshall, J., Peylin, P., Ayar, P. V., Ehret, G., Bréon, F.-M., Chevallier, F., Crevoisier, C., Gibert, F., Rairoux, P., Kiemle, C., Armante, R., Bès, C., Cassé, V., Chinaud, J., Chomette, O., Delahaye, T., Edouart, D., Estève, F., Fix, A., Friker, A., Klonecki, A., Wirth, M., Alpers, M., Millet, B. (2018). Error Budget of the MEthane Remote LI-dar missioN and Its Impact on the Uncertainties of the Global Methane Budget, J. Geophys. Res.-Atmos., 123, 11766–11785, https://doi.org/10.1029/2018JD028907

Bruhwiler, L. M., Basu, S., Bergamashi, P., Bousquet, P., Dlugokencky, E., Houweling, S., Ishizawa, M., Kim, H. S., Locatelli, R., Maksyutov, S., Montzka, S., Pandey, S., Patra, P. K., Pétron, G., Saunois, M., Sweeney, C., Schwietzke, S., Tans, P., Weatherhead, E. C. (2017). U.S. CH_4 emissions from oil and gas production: Have recent large increases been detected? *J. Geophys. Res.-Atmos., 122, 4070-4083,* https://doi.org/10.1002/2016JD026157

Butenhoff, C. L., Khalil, M. A. K. (2002). Correction for water vapor in the measurement of atmospheric trace gases. *Chemosphere, 47 (8),* 823-836, https://doi.org/10.1016/S0045-6535(01)00298-3

Cambaliza, M. O. L., Shepson, P. B., Caulton, D. R., Stirm, B., Samarov, D., Gurney, K. R., Turnbull, J., Davis, K. J., Possolo, A., Karion, A., Sweeney, C., Moser, B., Hendricks, A., Lauvaux, T., Mays, K., Whetstone, J., Huang, J., Razlivanov, I., Miles, N. L., Richardson, S. J. (2014). Assessment of uncertainties of an aircraft-based mass balance approach for quantifying urban greenhouse gas emissions. *Atmos. Chem. Phys.,* 14, 9029-9050, https://doi.org/10.5194/acp-14-9029-2014

Chen, H., Winderlich, J., Gerbig, C., Hoefer, A., Rella, C. W., Crosson, E. R., Pelt, A. D., Steinbach, J., Kolle, O., Beck, V., Daube, B. C., Gottlieb, E. W., Chow, V. Y., Santoni, G. W., Wofsy, S. C. (2010). High-accuracy continuous airborne measurements of greenhouse gases (CO_2 and CH_4) using the cavity ring-down spectroscopy (CRDS) technique. *Atmos. Meas. Tech 3,* 375-386, https://doi.org/10.5194/amt-3-375-2010

Ciais, P., Sabine, C., Bala, G., Bopp, L., Brovkin, V., Canadell, J., Chhabra, A., DeFries, R., Galloway, J., Heimann, M., Jones, C., Le Quéré, C., Myneni, R. B., Piao, S., Thornton, P. (2013). The physical science basis, contribution of working group 1 to the fifth assessment report of the intergovernmental panel on climate change, edited by: Stocker, T. F., Qin, D., Plattner, G. K., Tignor, M., Allen, S. K., Boschung, J., Nauels, A., Xia, Y., Bex, V., and Midgley, P. M. Cambridge University Press, Cambridge, UK, New York, NY, USA.

Di Piazza, A., Lo Conti, F., Noto, L. V., Viola, F., La Loggia, G. (2011). Comparative analysis of different techniques for spatial interpolation of rainfall data to create a serially complete monthly time series of precipitation for Sicily, Italy. *International Journal of Applied Earth Observation and Geoinformation. 13(*3). 396-408, https://doi.org/10.1016/j.jag.2011.01.005

Dosio, A., & de Arellano, J. V.-G. (2006). Statistics of Absolute and Relative Dispersion in the Atmospheric Convective Boundary Layer: A Large-Eddy Simulation Study. *Journal of the Atmospheric Sciences*, 63(4), 1253–1272. https://doi.org/10.1175/JAS3689.1

Edwards, T. D., Wong, Y. K., Jeong, C. H., Wang, J. M., Su, Y., Evans, G. J. (2025). Comparison of methods for resolving the contributions of local emissions to measured concentrations. *Atmos. Meas. Tech. 18*(9), p2201-2240, https://doi.org/10.5194/amt-18-2201-2025

Han, T., Xie, C., Lui, Y., Yang, Y., Zhang, Y., Huang, Y., Gao, X., Zhang, X., Bao, F., Li, S. M. (2024). Development of a continuous UAV-mounted air sampler and application to the quantification of CO_2 and CH_4 emissions from a major coking plant, *Atmos. Meas. Tech. 17(*2), 677-691. https://doi.org/10.5194/amt-17-677-2024

Hooghiem, J. J. D., de Vries, M., Been, H. A., Heikkinen, P., Kivi, R., Chen, H. (2018). LISA: a lightweight stratospheric air sampler. *Atmos. Meas. Tech* 11(12), pp. 6785–6801. https://doi.org/10.5194/amt-11-6785-2018

ICOS (2020). *ICOS ATC Metrology Laboratory Evaluation report for the LICOR LI-7810 instrument; ICOS ATC Website:* https://icos-atc.lsce.ipsl.fr/docs

Karion, A., Sweeney, C., Pétron, G., Frost, G., Michael Hardesty, R., Kofler, J., Miller, B. R., Newberger, T., Wolter, S., Banta, R., Brewer, A., Dlugokencky, E., Lang, P., Montzka, S. A., Schnell, R., Tans, P., Trainer, M., Zamora, R., and Conley, S. (2013). Methane emissions estimate from airborne measurements over a western United States natural gas field, Geophysical Research Letters, 40, 4393–4397, https://doi.org/10.1002/grl.50811

Kim, J., Seo, B.-k., Lee, T., Kim, J., Kim, S., Bae, G.-N., & Lee, G. (2023). Airborne estimation of SO2 emissions rates from a coal-fired power plant using two top-down methods: A mass balance model and Gaussian footprint approach. Science of the Total Environment, 855. https://doi.org/10.1016/j.scitotenv.2022.158826

Kunz, M., Lavric, J.V., Gerbig, C., Tans, P., Neff, D., Hummelgård, C., Martin, H., Rödjegård, H., Wrenger, B., Heimann, M. (2018). COCAP: a carbon dioxide analyser for small unmanned aircraft systems. *Atmos. Meas. Tech. 11* (3), 1833–1849. https://doi.org/10.5194/amt-11-1833-2018.

Leitner, S., Feichtinger, W., Mayer, S., Mayer, F., Krompetz, D., Hood-Nowotny, R., Watzinger, A. (2023). UAV-based sampling systems to analyse greenhouse gases and volatile organic compounds encompassing compound-specific stable isotope analysis. *Atmos, Meas. Tech.* 16, 513-527. https://doi.org/10.5194/amt-16-513-2023.

Leytem, A. B., Bjorneberg, D. L., Koehn, A. C., Moraes, L. E., Kebreab, E., Dungan, R. S. (2017). Methane emissions from dairy lagoons in the western United States. *Journal of Airy Science, 100(*8). 6785-6803. https://doi.org/10.3168/jds.2017-12777

Mohammadloo, T. H., Jones, M., van de Kerkhof, B., Dawson, K., Smith, B. J., Conley, S., Corbett, A., Ijzermans, R. (2025). Quantitative estimate of several sources of uncertainty in drone-based methane emissions measurements. *Atmos. Meas. Tech. 18*(5). 1301-1324. https://doi.org/10.5194/amt-18-1301-2025

Morales, R., Ravelid, J., Vinković, K., Korben, P., Tuszon, B., Emmenegger, L., Chen, H., Schmidt, M., Humbel, S., Brunner, D. (2022). Controlled-release experiment to investigate uncertainties in UAV-based emission quantification for methane point sources. *Atmos. Meas. Tech.* 15, 2177-2198. https://doi.org/10.5194/amt-15.2177-2022.

Nathan, B.J., Golston, L.M., O'Brien, A.S., Ross, K., Harrison, W.A., Tao, L., Zondlo, M.A. (2015). Near-field characterization of methane emission variability from a Compressor Station using a model aircraft. Environ. Sci. Technol. 49 (13), 7896–7903. https://doi.org/10.1021/acs.est.5b00705.

Ražnjević, A., van Heerwaarden, C., & Krol, M. (2022). Evaluation of two common source estimation measurement strategies using large-eddy simulation of plume dispersion under neutral atmospheric conditions. Atmospheric Measurement Techniques, 15(11), 3611–3628. https://doi.org/10.5194/amt-15-3611-2022

Saunois, M., Stavert, A. R., Poulter, B., Bousquet. P., Canadell, J. G., Jackson, R. B., Raymond, P. A., Dulgokencky, E. J., Houweling, S., Patra, P. K., Ciais, P., Arora, V. K., Bastviken, D., Bergamaschi, P., Blake, D. R., Brailsford, G., Bruhwiler, L., Carlson, K. M., Carrol, M., … Zhuang, Q. (2020). The global methane budget 2000-2017. *Earth Syst. Sci. Data, 12,* 1561-1623. https://doi.org/10.5194/essd-12-1561-2020

Shah, A., Pitt, J. R., Ricketts, H., Brian Leen, J., Williams, P. I., Kabbabe, K., Gallagher, M. W., Allen, G. (2020). Testing the near-field Gaussian plume inversion flux quantification technique using unmanned aerial vehicle sampling. *Atmos. Meas. Tech.* 13, 1467-1484. https://doi.org/10.5194/amt-13-1467-2020

Shaw, J. T., Shah, A., Yong, H., Allen, G. (2021). Methods for quantifying methane emissions using unmanned aerial vehicles: a review. *Philos. Trans. R. Soc. A Math. Phys. Eg. Sci.* 379. https://doi.org/10.1098/rsta.2020.0450

Stull, R. B. (1988). An introduction to boundary layer meteorology (1st ed.) [Printed version]. Kluwer Academic Publishers. https://doi.org/10.1007/978-94-009-3-27-8

Uhlenbeck, G. E., Ornstein, L. S. (1930). On the theory of the Brownian motion. *Phys. Re. 36,* 823. https://doi.org/10.1103/PhysRev.36.823

United Nations Environment Programme (UNEP) and Climate and Clean Air Coalition (CACC). (2021). Global Methane Assessment: Benefits and Costs of Mitigation Methane Emissions. *Nairobi: United Nations Environment Programme* ISBN: 978-92-807-3854-4

VanderZaag, A. C., Gordon, R. J., Jamieson, R. C., Burton, D. L., Stratton, G. W. (2010). Effects of winter storage and subsequent agitation on gaseous emissions from liquid dairy manure. *Can. J. Soil. Sci. 90*(1): 229-239. https://doi.org/10.4141/CJSS09040

Vechi, M. T., Falk, J. M., Fredenslund, A. M., Edjabou, M. E., Scheutz, C. (2023). Methane emission rates averaged over a year from ten farm-scale manure storage tanks. *Science of the Total Environment, 904*, Article 1666610. https://doi.org/10.1016/j.scitotenv.2023.166610

Vinković, K., Andersen, T., de Vries, M., Kers, B., van Heuven, S., Peters, W., Hensen, A., van den Bulk, P., Chen, H. (2022). Evaluating the use of an Unmanned Aerial Vehicle (UAV)-based active AirCore system to quantify methane emissions from dairy cows. *Science of the Total Environment*, *831*(March). https://doi.org/10.1016/j.scitotenv.2022.154898

Wieringa, J. (1992). Updating the Davenport roughness classification. *Journal of Wind Engineering and Industrial Aerodynamics. Vol. 43(*1-3), 357-368. https://doi.org/10.1016/0167-6105(92)90434-C

Wietzel, J. B., Korben, P., Hoheisel, A., Schmidt, M. (2025). Best practices and uncertainties in CH_4 emission quantification: emplying mobile measurements and Gaussian plume moddeling at a biogas plant. *Atmos. Meas. Tech. 18*(18). 4631-4645. https://doi.org/10.5194/amt-18-4631-2025

World Meteorological Organization (WMO). (2025). WMO Greenhouse Gas Bulletin. No. 21 https://library.wmo.int/idurl/4/69654

Yong, H., Allen, G., Mcquilkin, J., Ricketts, H., & Shaw, J. T. (2024). Lessons learned from a UAV survey and

915 methane emissions calculation at a UK landfill. *Waste Management (New York, N.Y.)*, *180*, 47–54. https://doi.org/10.1016/j.wasman.2024.03.025

7 Appendix

7.1 Temperature control during flight (A)

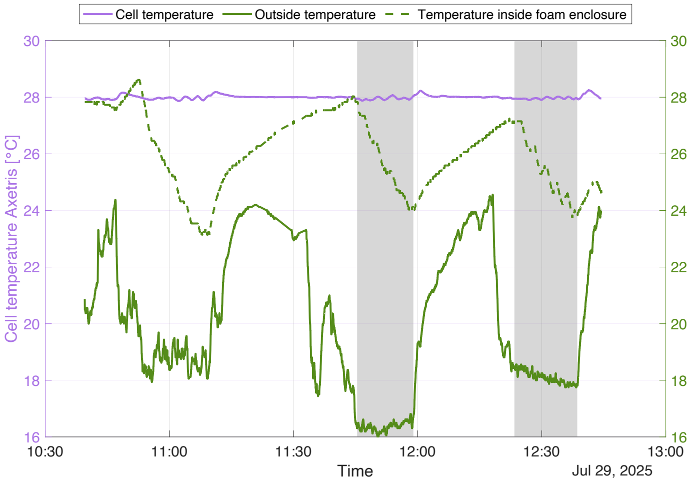

920

Figure A1: Temperature stability during the flight one and two. The actively controlled temperature recorded by the Axetris sensor is shown in purple (left axis; set to 28°) The shaded regions indicate the flight periods. The solid green line denotes the ambient air temperature, while the dashed green line shows the temperature of the PBD inside the foam enclosure (right axis).

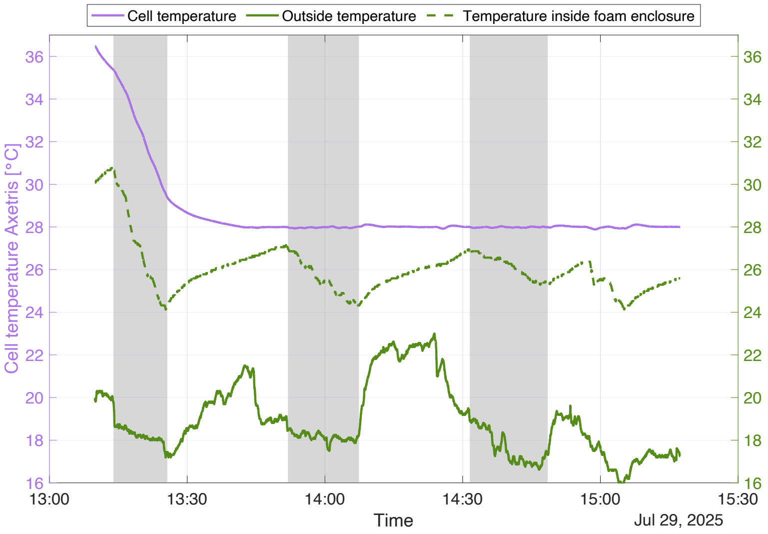

925 *Figure A2: Temperature stability during the flight three, four and five. The actively controlled temperature recorded by the Axetris sensor is shown in purple (left axis; set to 28°) The shaded regions indicate the flight periods. The solid green line*

denotes the ambient air temperature, while the dashed green line shows the temperature of the PBD inside the foam enclosure (right axis). Prior to this measurement series, the Axetris was accidently heated to 36°C. The rapid cooling during flight, severely affected Axetris readings.

930

7.2 Linearity test (B)

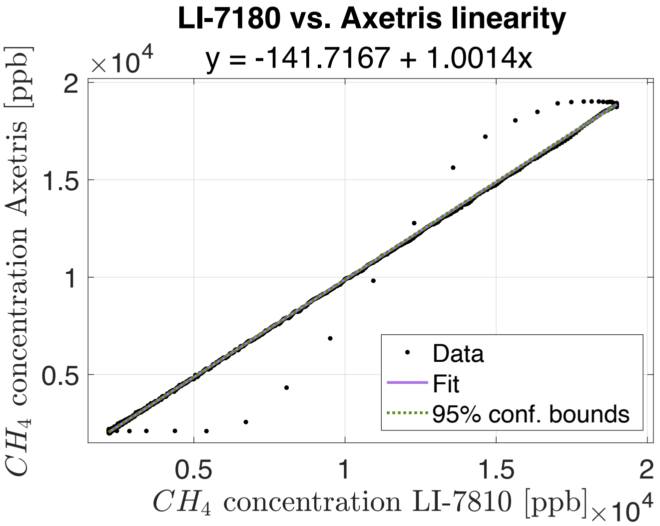

Figure B1: Linear regression plot showing the linearity between LI-7180 and Axetris data. The outliers are due to differences in response time.

935

7.3 Experimental setup of the water vapour test (C)

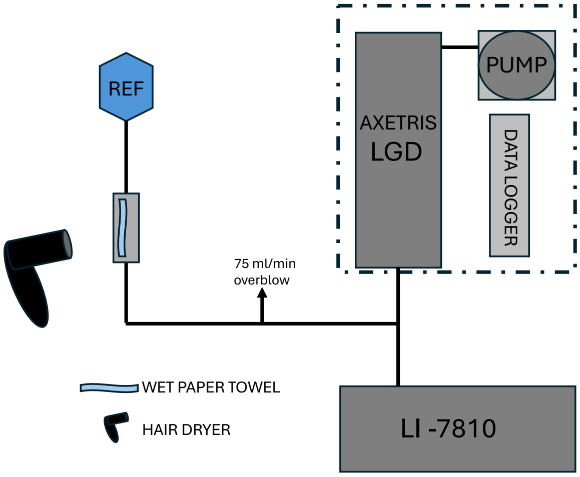

Figure C1: Overview of the water droplet test setup. A wet paper towel is placed in an enclosed Swagelok compartment, and the reference gas used had a high CH_4 concentration (±81 ppm). The compartment can be heated, thereby increasing the water vapour concentration relative to the reference gas.

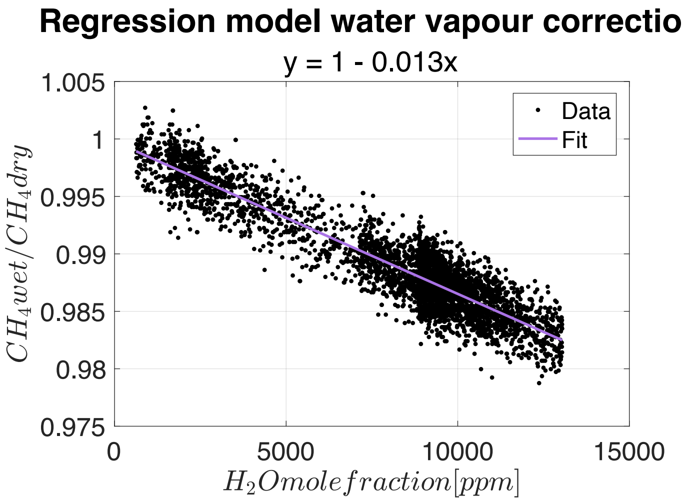

Figure C2: Regression model used to determine the water vapour correction as described in section 2.4. The linear relationship between the wet and dry fractions can be used to correct for water vapour during field experiments. The R^2 value is 0.86, and the RMSE is 0.0016.

7.4 Meteorological data (D)

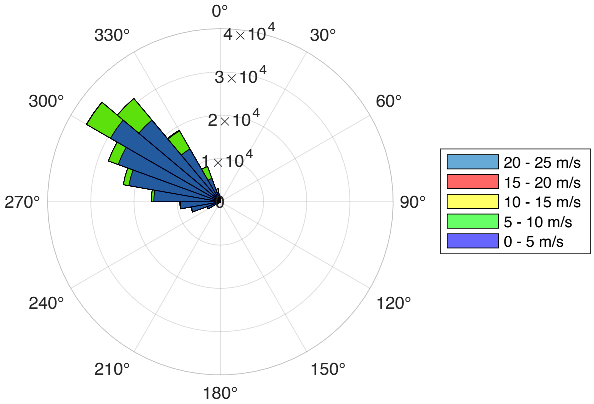

Figure D1: Wind rose of 3D sonic observations during the campaign day at 29-07-2025.

https://doi.org/10.5194/egusphere-2025-6209
Preprint. Discussion started: 21 January 2026

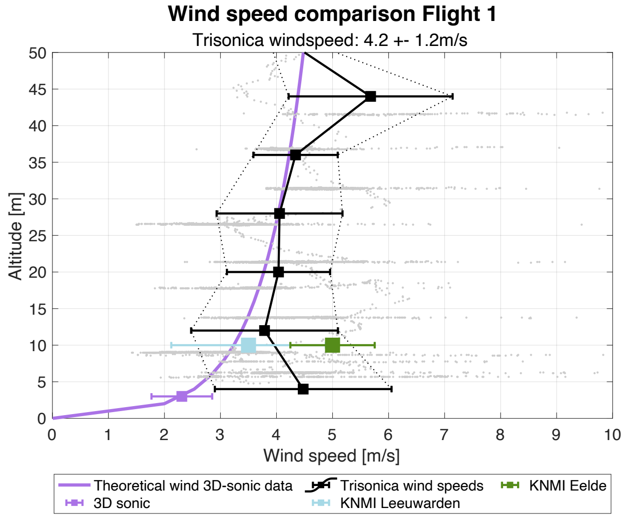

Figure D2: compilation of wind speed information during Grijpskerk flight 1. Shown are a theoretical, exponential wind speed profile (purple line) anchored by measured data from the 3D sonic at 3 m altitude (purple marker) and the individual (light gray) and bin-averaged (black) TriSonica wind speed data collected by the drone. The mean wind speed during flight observed 955 by the TriSonica was 4.2 m/s ± 1.2 m/s. Additional markers show KNMI observations from nearby stations Eelde (green) and Leeuwarden (blue).

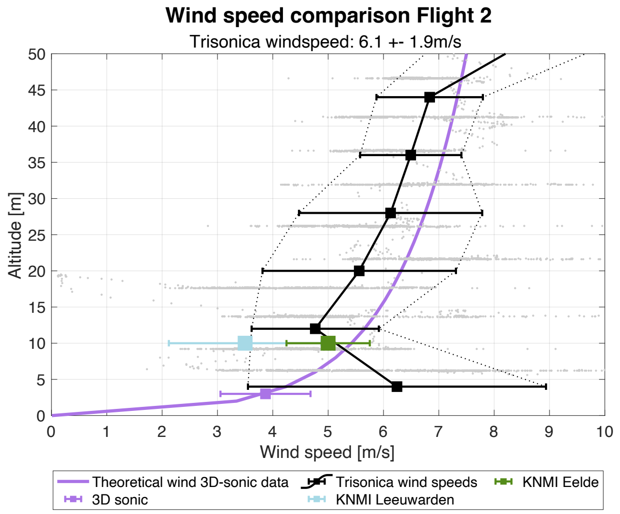

Figure D3: compilation of wind speed information during Grijpskerk flight 2. Shown are a theoretical, exponential wind speed 960 profile (purple line) anchored by measured data from the 3D sonic at 3 m altitude (purple marker) and the individual (light gray) and bin-averaged (black) TriSonica wind speed data collected by the drone. The mean wind speed during flight observed by the TriSonica was 6.1 m/s ± 1.9 m/s. Additional markers show KNMI observations from nearby stations Eelde (green) and Leeuwarden (blue).

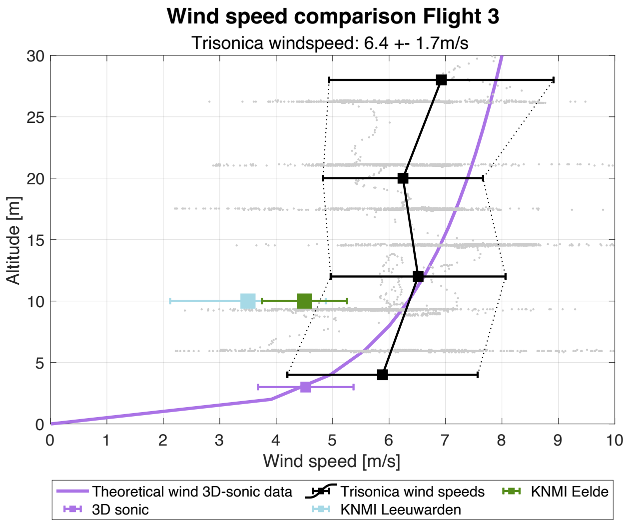

965

Figure D4: compilation of wind speed information during Grijpskerk flight 3. Shown are a theoretical, exponential wind speed profile (purple line) anchored by measured data from the 3D sonic at 3 m altitude (purple marker) and the individual (light gray) and bin-averaged (black) TriSonica wind speed data collected by the drone. The mean wind speed during flight observed by the TriSonica was 6.4 m/s ± 1.7 m/s. Additional markers show KNMI observations from nearby stations Eelde (green) and 970 *Leeuwarden (blue).*

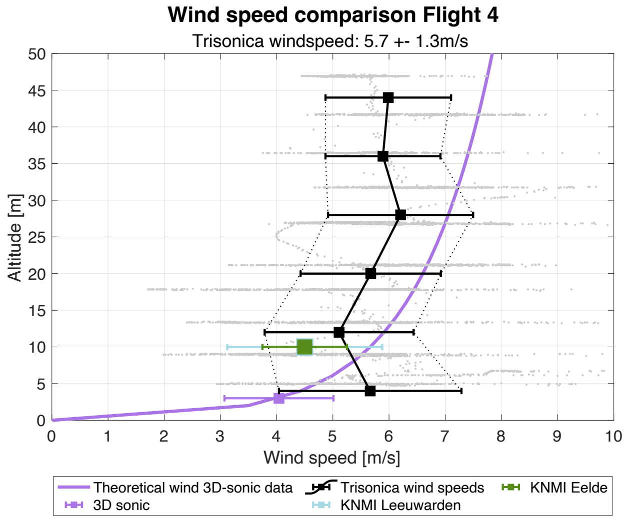

Figure D5: compilation of wind speed information during Grijpskerk flight 4. Shown are a theoretical, exponential wind speed profile (purple line) anchored by measured data from the 3D sonic at 3 m altitude (purple marker) and the individual (light gray) and bin-averaged (black) TriSonica wind speed data collected by the drone. The mean wind speed during flight observed 975 *by the TriSonica was 5.7 m/s ± 1.3 m/s. Additional markers show KNMI observations from nearby stations Eelde (green) and Leeuwarden (blue).*

https://doi.org/10.5194/egusphere-2025-6209
Preprint. Discussion started: 21 January 2026

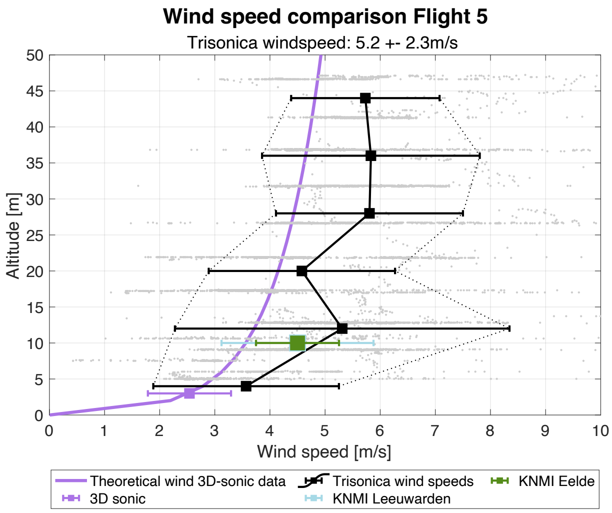

Figure D6: compilation of wind speed information during Grijpskerk flight 5. Shown are a theoretical, exponential wind speed profile (purple line) anchored by measured data from the 3D sonic at 3 m altitude (purple marker) and the individual (light gray) and bin-averaged (black) TriSonica wind speed data collected by the drone. The mean wind speed during flight observed by the TriSonica was 5.2 m/s ± 2.3 m/s. Additional markers show KNMI observations from nearby stations Eelde (green) and Leeuwarden (blue).

7.5 Background determination (E)

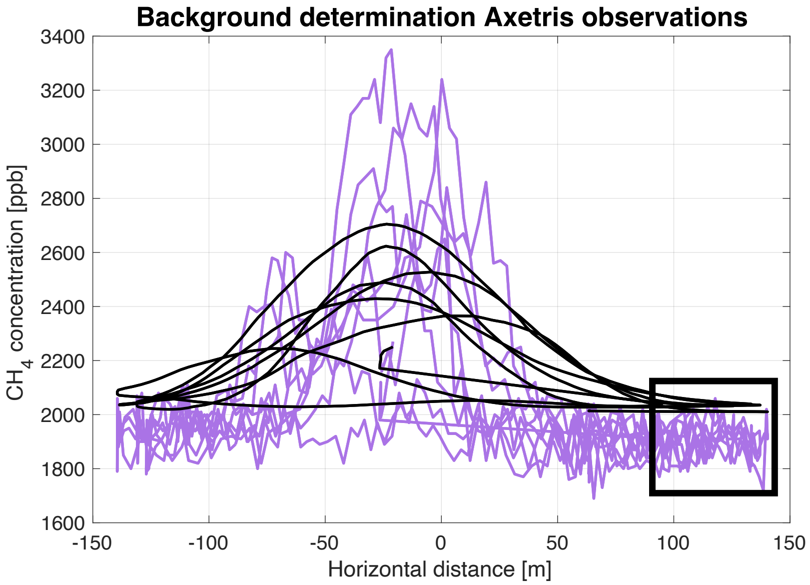

Figure E1: Method to determine the plume boundaries and background concentration of the Axetris observations (purple) and the AirCore observations (black) of flight 1. The enclosed area is thought to contain the background of the Axetris, and the average value is determined by isolating the specific observations

7.6 Correlation Axetris vs. AirCore observations (F)

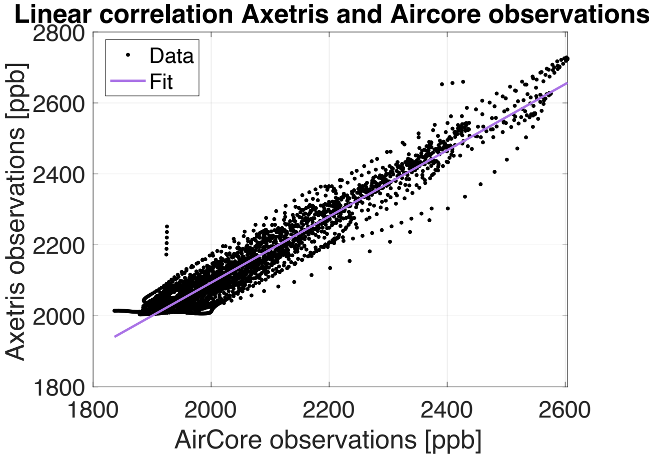

Figure F1: Linear correlation plot of the smoothed Axetris observations compared to the activeAirCore observations. All flight observations (with the exception of flight 3) are considered in this plot. The linear correlation coefficient is R^2=0.936 and an RMSE of 37.9 is found.

7.7 Curtain orientation (G)

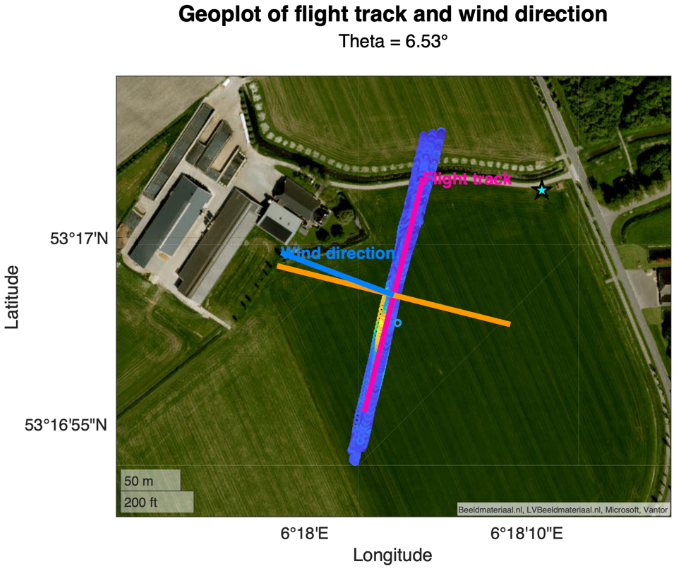

Figure G1: Top-down view of the flight track and CH_4 observations of the Axetris during flight 1. Figure used to determine the angular deviation between the perpendicular line (orange line) of the mean flight track (pink line) and the wind direction (blue). The blue star represents the position of the WindMaster Pro.

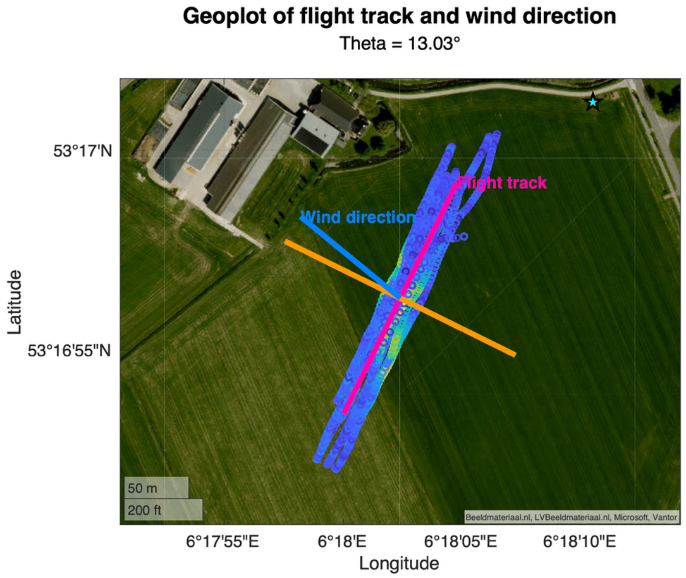

Figure G2: Top-down view of the flight track and CH₄ observations of the Axetris during flight 1. Figure used to determine the angular deviation between the perpendicular line (orange line) of the mean flight track (pink line) and the wind direction (blue). The blue star represents the position of the WindMaster Pro.

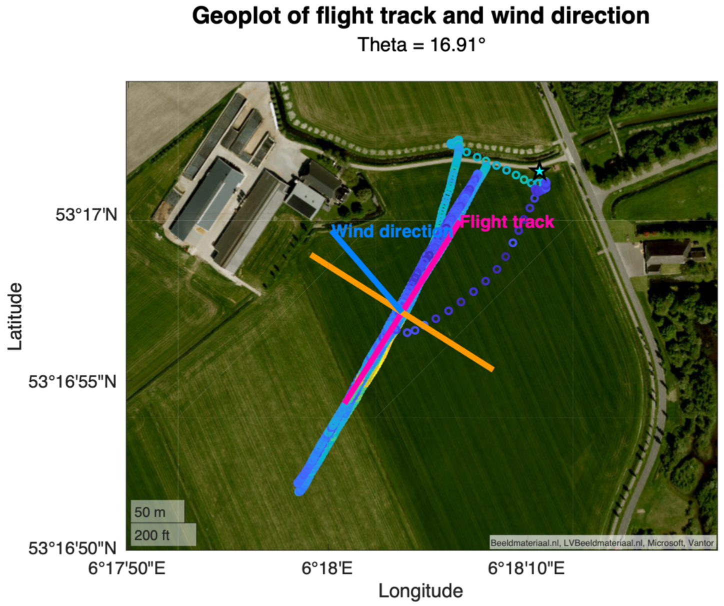

Figure G3: Top-down view of the flight track and CH₄ observations of the Axetris during flight 3. Figure used to determine the angular deviation between the perpendicular line (orange line) of the mean flight track (pink line) and the wind direction (blue). The blue star represents the position of the WindMaster Pro.

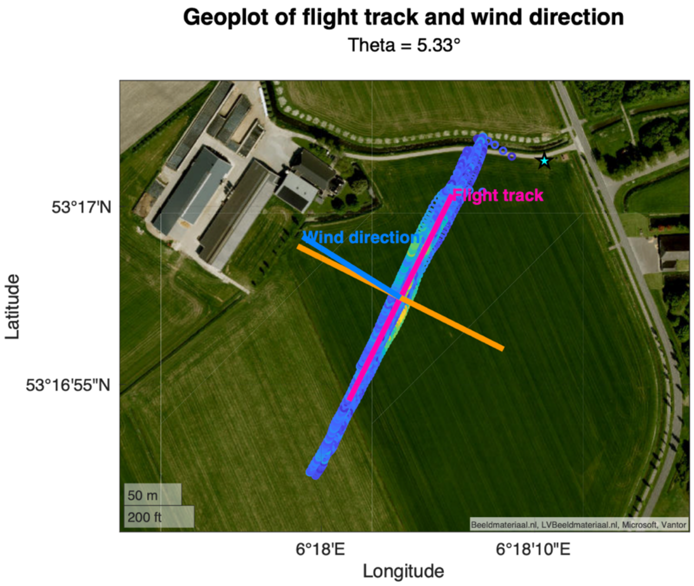

1010 *Figure G4: Top-down view of the flight track and CH₄ observations of the Axetris during flight 4. Figure used to determine the angular deviation between the perpendicular line (orange line) of the mean flight track (pink line) and the wind direction (blue). The blue star represents the position of the WindMaster Pro.*

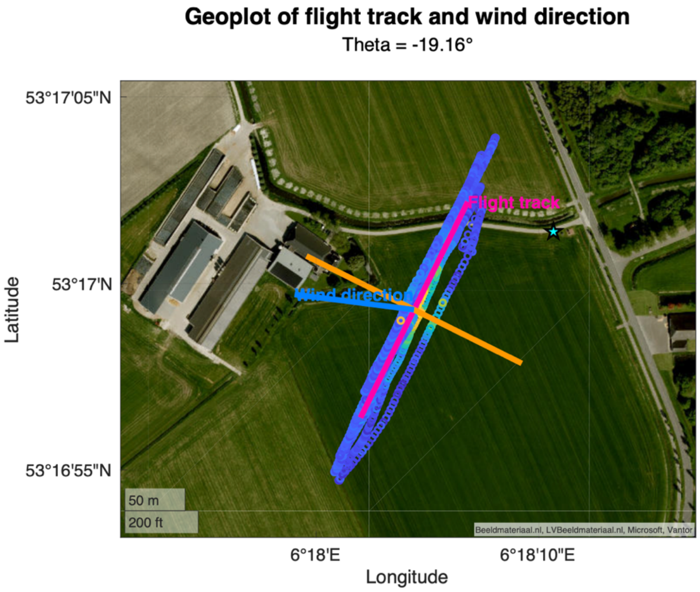

1015 *Figure G5: Top-down view of the flight track and CH₄ observations of the Axetris during flight 5. Figure used to determine the angular deviation between the perpendicular line (orange line) of the mean flight track (pink line) and the wind direction (blue). The blue star represents the position of the WindMaster Pro.*

7.8 All flight profiles (H)

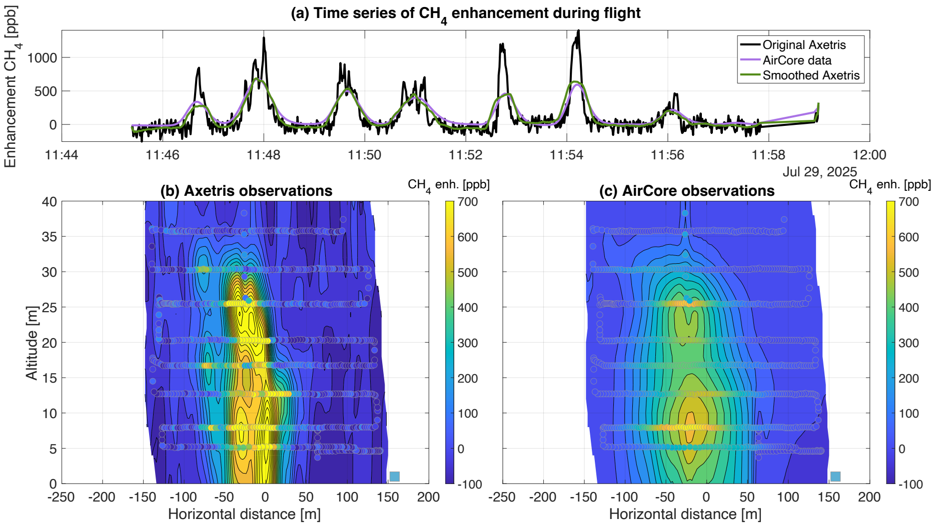

1020

Figure H1: Overview of the observed CH$_4$ enhancements and spatial interpolation of flight 1. Estimated flux of Axetris 2.8 gCH$_4$/s (B); AirCore 3.5 gCH$_4$/s (C)

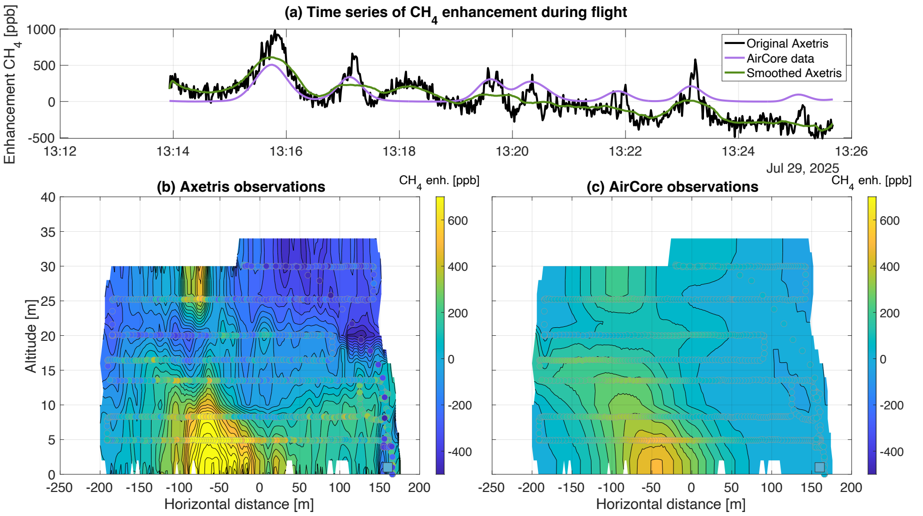

1025 Figure H2: Overview of the observed CH$_4$ enhancements and spatial interpolation of flight 3. During the flight, the temperature control malfunctioned. This flight was left entirely out of the analysis

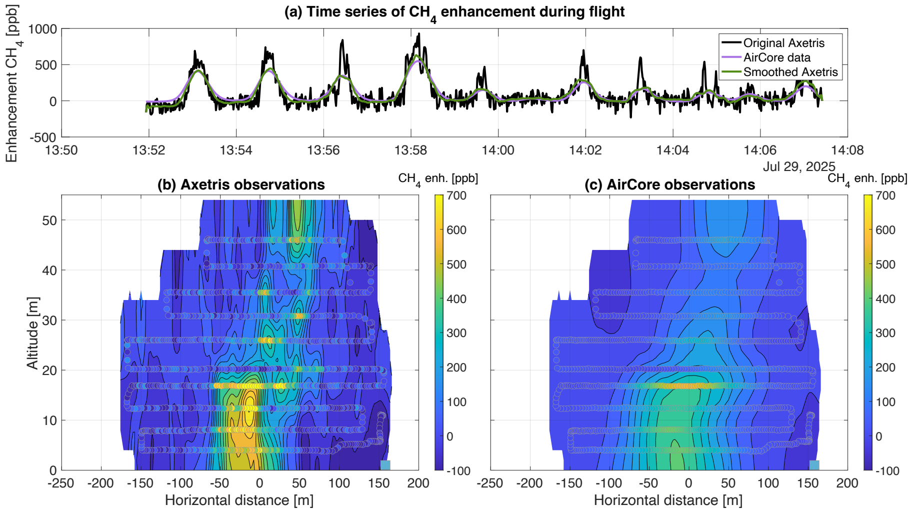

Figure H3: Overview of the observed CH_4 enhancements and spatial interpolation of flight 4. Estimated flux of Axetris 5.4 gCH_4/s (B); AirCore 5.0 gCH_4/s (C)

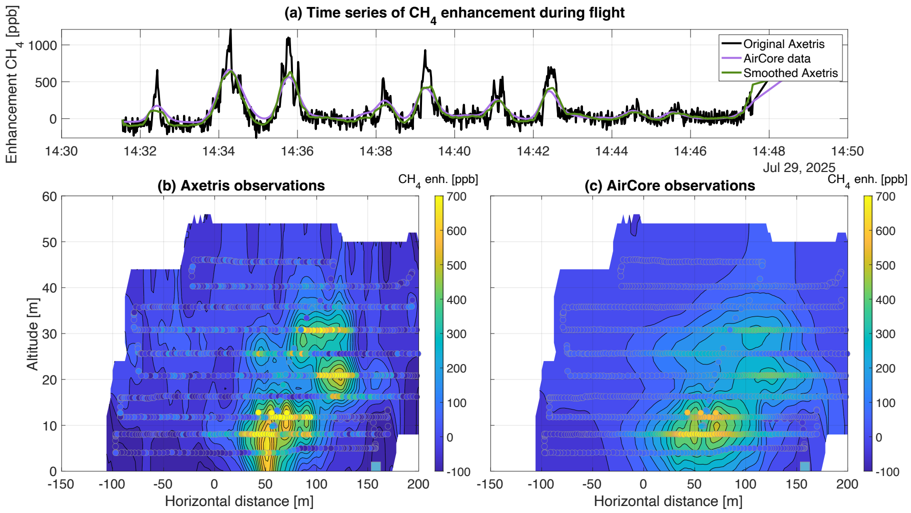

Figure H4: Overview of the observed CH_4 enhancements and spatial interpolation of flight 5. Estimated flux of Axetris 2.8 gCH_4/s (B); AirCore 3.0 gCH_4/s (C)

https://doi.org/10.5194/egusphere-2025-6209
Preprint. Discussion started: 21 January 2026

7.9 Plume simulation results (I)

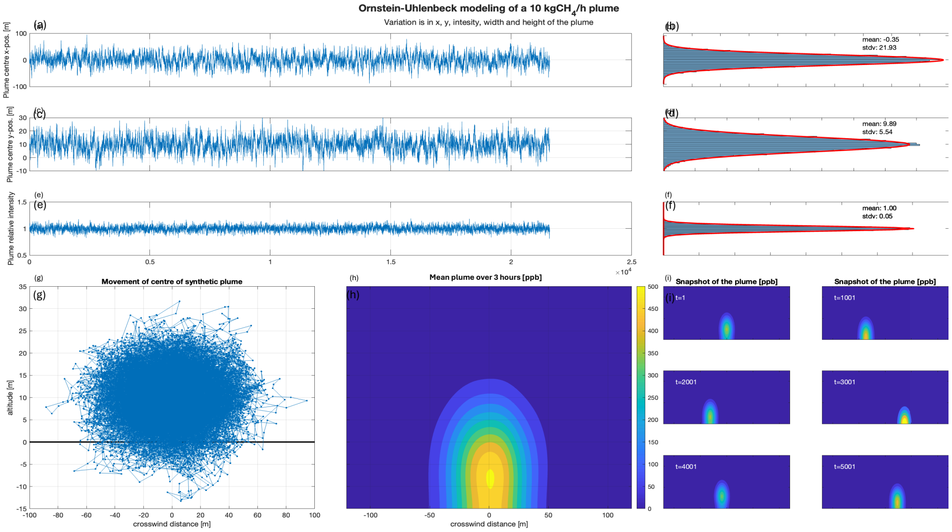

Figure I1: Stochastic plume simulation using the Ornstein-Uhlenbeck model to simulate a plume of 10 kgCH$_4$/hr. The top three figures (a-f) depict the time series fluctuations of the plumes horizontal and vertical position and plume intensity and spread are presented, together with the probability distribution of these parameters; (g) The simulated trajectory of the plume around the centerline motion; (h) the spatial interpolation of the 3 hour averaged plume; (i) example of instantaneous plume snapshots